The timing of collision between Asia and the West Burma Terrane, and the development of the Indo-Burman Ranges

Yani Najman[1], Edward R. Sobel[2], Ian Millar[3], Xiwu Luan[4*], Sebastian Zapata[5], Eduardo Garzanti[6], Mauricio Parra[7], Giovanni Vezzoli[6], Peng Zhang[8], Day Wa Aung[9], Saw Mu Tha Lay Paw[10], Thae Naung Lwin[9].

*Corresponding author. Email: xluan@sdust.edu.cn

[1] Lancaster Environment Centre, Lancaster University, LA1 4YQ, UK.

[2] Institute of Geosciences, Universitat Potsdam, 14476 Potsdam-Golm, Germany.

[3] NERC Isotope Geosciences Lab, BGS Keyworth, NG12 5GG, UK.

[4] College of Earth Science and Engineering, Shandong University of Science and Technology, Qingdao, China.

[5] Smithsonian Tropical Research Institute, Center for Tropical Paleocology and Archaeology, Panama.

[6] Department of Earth and Environmental Sciences, Università di Milano-Bicocca, Milano 20126, Italy

[7] Universidada de Sao Paulo, Institute for Energy and Environment, Brazil

[8] China University of Geosciences, Wuhan, China.

[9] Geology Department, University of Yangon, Pyay Rd, Yangon, Myanmar

[10] independent

Abstract

The West Burma Terrane (WBT) is a small terrane bounded to the east by the Asian Sibumasu Block and to the west by the Indo-Burman Ranges (IBR), the latter being an exhumed accretionary prism that formed during subduction of Indian oceanic lithosphere beneath Asia. Understanding the geological history of the WBT is important for reconstruction of the closure history of the Tethys ocean and India-Asia collision. Currently there are major discrepancies in the proposed timings of collision between the WBT with both India and Asia; whether the WBT collided with India or Asia first is debated, and proposed timings of collisions stretch from the Mesozoic to the Cenozoic. We undertook a multi-technique provenance study involving petrography, detrital zircon U-Pb and Hf analyses, rutile U-Pb analyses and Sr-Nd bulk rock analyses on sediments of the Central Myanmar Basins (CMB) of the WBT. We determined that the first arrival of Asian material into the basin occurred after the earliest late Eocene and by the early Oligocene, thus placing a minimum constraint on the timing of WBT-Asia collision. Our low temperature thermochronological study of the IBR record two periods of exhumation, in the early-middle Eocene, and at the Oligo-Miocene boundary. The Eocene event may be associated with the collision of the WBT with India. The later event at the Oligo-Miocene boundary may be associated with changes in wedge dynamics resulting from increased sediment supply to the system; however a number of other possible causes provide equally plausible explanations for both events.

1. Introduction

The West Burma Terrane (WBT, Fig 1) is a small terrane, roughly coincident with the geographic borders of Myanmar. It consists of the Cretaceous-Cenozoic Wuntho-Popa Arc (WPA) and associated Central Myanmar forearc and backarc basins (CMB), separated from the Asian Sibumasu terrane to the east by the Sagaing Fault, and flanked to the west by the exhumed accretionary prism of the Indo-Burman Ranges (IBR).

Knowledge of the evolution of the WBT is important for understanding the geological history of the closure of the Tethys Ocean and stages of the India-Asia collision. Yet our current understanding is rudimentary. From Palaeozoic times onwards, various continental fragments including the WBT rifted from Gondwana and drifted north across the Tethys, accreting to the southern margin of Asia. Within this context, a number of researchers consider that the WBT was part of Asia by early Mesozoic or early Cenozoic times (see discussion in *Barber et al.* [2017]; [*Hall*, 2012]), which subsequently collided with India. Conversely, new palaeomagnetic data suggests that the WBT lay at 5° S in the Late Cretaceous and 4° N in the late Eocene; the WBTand collided with India in the early Cenozoic, followed by later collision with Asia [*Westerweel et al.*, 2019, and see also Morley et al (2020)]. However, as pointed out by *Morley et al.* [2021], this Late Eocene location requires rapid northward motion of the WBT in order for the terrane to reach its present position; such a trajectory should have left clear evidence of tectonic activity between the eastern margin of the WBT and the Asian margin of Sibumasu, which is not clearly observed.

In this paper we investigate two aspects of the geology of the WBT that can be used to constrain the geological history of the terrane. First we research the provenance of the CMB, using it to determine when Asian material first arrived on the WBT and thus place constraints on when the two blocks collided. Previous work has proposed first arrival of

Asian material into the CMB in late Eocene times [*Licht et al.*, 2018], Oligocene times [*Arboit et al.*, 2021; *Zhang et al.*, 2021; *Zhang et al.*, 2019] or not until the Miocene [*Westerweel et al.*, 2020]. Second, we determine the timing of uplift of the IBR, exhumation of which has been debatably linked to collision of the WBT with India [e.g. *Aitchison et al.*, 2007; *Morley*, 2009; *Morley et al.*, 2020; *Verard et al.*, 2017]. Previous work has indicated there is tentative evidence of IBR exhumation in the Eocene, with more substantial exhumation around the Oligo-Miocene boundary [*Licht et al.*, 2018; *Najman et al.*, 2020].

In this study we undertook a second IBR age elevation transect >200 km north of our previous transect [*Najman et al.*, 2020], and undertook thermal modeling of data from our previous transect. We aimed to assess the regional cooling history and to determine if rapid exhumation of the IBR in the Eocene, as we previously tentatively proposed, could be confirmed. Secondly, we undertook more provenance analyses in the CMB to narrow the data gap over which the timing of first arrival of Asian material that we previously identified [*Zhang et al.*, 2019] occurred.

2. Geological background

2.1 Geology of Myanmar

The geomorphology of Myanmar, closely tied to the geology, consists of four main divisions (Fig 1): the highlands to the north, the Shan Thai plateau to the east, the IBR to the west, and the CMB in the centre.

2.1.1 Sibumasu

Both the northern Highlands and the Shan Thai plateau are part of the Asian Sibumasu Block.

Low to high grade metamorphic rocks of the Mogok Metamorphic Belt (MMB) and spatially associated granites are located in the northern Highlands of Myanmar, with a thin sliver of MMB rocks trending north-south along the length of the eastern margin of the CMB, separated from it by the Sagaing Fault. Metamorphism occurred from latest Cretaceous to Early Miocene, interpreted to be associated with India-Sibumasu collision [*Barley et al.*, 2003; *Lamont et al.*, 2021; *Searle et al.*, 2020]. Subsequent cooling and exhumation took place in the Late Oligo-Miocene [*Bertrand et al.*, 2001]. The granitoids, such as the Dianxi-Burma Batholiths of the MMB and the Bomi-Chayu Batholiths of the Eastern Transhimalaya, are of Cretaceous-Paleogene age [e.g. *Liang et al.*, 2008]. Sibumasu's Shan-Thai plateau is separated from the CMB by the Sagaing Fault. It is characterised by Cambrian-Mesozoic clastic sedimentary rocks, limestones and subordinate volcanics [e.g. *A H G Mitchell et al.*, 2012]. On the western flank of the Shan Thai plateau, a thin sliver of MMB extends from the north.

2.1.2. The Indo-Burman Ranges (IBR)

The IBR is a north-south trending, west-vergent, thin-skinned fold-thrust belt [e.g. *P. M. Betka et al.*, 2018] located on the western margin of the WBT, adjacent to the CMB (Fig. 1). It is an exhumed accretionary prism affected by the hyper-oblique subduction of Tethyan lithosphere and final collision of India beneath and with the WBT [*Morley et al.*, 2020]. The

eastern Inner side of the IBR consists of Cretaceous-middle Eocene deep marine rocks (including the Falam Fm., Morley et al., 2020) and some ~Late Eocene-Oligocene? conglomerates [e.g. *Aitchison et al.*, 2019; *Ghose et al.*, 2014], whilst the western Outer belt extends to Neogene shallow marine and younger fluvial facies [e.g. *Naing et al.*, 2014]. The core of the IBR exposes Burmese "basement" of Kanpetlet schists, and its probable unmetamorphosed equivalent of the Triassic Pane Chaung turbidites [*Morley et al.*, 2020], as well as early Cretaceous ophiolitic fragments [e.g. *Sevastjanova et al.*, 2015; *Socquet et al.*, 2002]. Major Cenozoic structures within the Burmese portion of the range include the Kabaw, Kheng, and Kaladan faults. In our study area, deformation is driven by folds and west-vergent thrusts that have a component of dextral transpression [e.g. *A H G Mitchell et al.*, 2010; *Morley et al.*, 2020]. Our profile crosses four faults, discussed in section 4.1.1.

2.1.3. The Central Myanmar Basins (CMB)

The CMB is a forearc-backarc basin couplet divided by the mid Cretaceous-Eocene Wuntho Popa arc (WPA) [e.g. *Licht et al.*, 2020; *P Zhang et al.*, 2017]. The forearc is divided into the Chindwin Sub-basin to the north and the Minbu Sub-basin to the south. The backarc is subdivided into the Shwebo, northern Minwun and Myitkina-Katha Sub-basins to the north and the Pegu Basin to the south. According to *Licht et al.* [2018], the forearc basins were partitioned, with different geological histories, from late Eocene times. Today, the Ayeyawady (Irrawaddy) River flows down the CMB from its headwaters in the MMB to the north of the basin.

In the forearc, marine facies predominate from Albian to middle Eocene times in both north and south sub-basins, becoming fluvio-deltaic to continental in the overlying Pondaung

Formation. However, from the time of deposition of the Yaw Formation at the middle-late Eocene boundary [*Licht et al.*, 2018], Licht et al. (2018) record divergence; the Yaw Formation in the Minbu Basin is exclusively shallow marine, whilst in the Chindwin basin it is both marine and continental. Above the Yaw formation there is an unconformity in the Chindwin Basin but not in the Minbu Basin where sedimentation continued with the deposition of the Oligocene Shwezetaw, Padaung and Okhmintaung Formation. The Chindwin Basin records fluvial facies from late Oligocene times onwards, whilst mixed shallow marine and deltaic facies persist in the Oligocene in the Minbu Basin, passing up to fluvio-deltaic facies in the early Miocene, with fluvial facies beginning in the late middle Miocene to Pliocene. In the Chindwin Basin, Westerweel et al. (2020) diverges from Licht et al. (2018) by further dividing the Letkat Formation into the upper Oligocene Tonhe Formation and overlying lower Miocene Letkat Formation, divided by an unconformity of earliest Miocene duration. Backarc facies changes are approximately coeval to those of the forearc, where known. Table 1 illustrates the basin stratigraphy in detail.

2.2 Previous work on the provenance history of the CMB

Previous work on the CMB has focussed on zircon U-Pb analyses to allow discrimination between Mesozoic-Cenozoic arc-derived grains versus older crustal input [*Cai et al.*, 2020; *Licht et al.*, 2018]. Hf-isotope characterisation of these Mesozoic-Cenozoic grains allows for discrimination between zircons from the WPA, which have positive εHf values, as opposed to grains of similar age from the MMB, which have negative values [*Wang et al.*, 2014; *Zhang et al.*, 2019]. Other techniques have included rutile U-Pb analyses, with Cenozoic grains interpreted as derived from the MMB [*Zhang et al.*, 2019], and rutile geochemistry to

assess metamorphic grade [*Arboit et al.*, 2021]. *Arboit et al.* [2021] also applied U-Pb thermochronology to titanite and apatite, the latter also including trace element geochemistry, to determine the source region's timing of cooling and grade of metamorphism. Sr-Nd bulk analyses [*Licht et al.*, 2014; *Licht et al.*, 2013; *Zhang et al.*, 2019] documented changing proportions of arc versus crustal material through time, and petrographic data has also been used to assess changes in source region [*Cai et al.*, 2020; *Licht et al.*, 2014; *Licht et al.*, 2013; *Wang et al.*, 2014; *Zhang et al.*, 2019].

The overwhelming predominance of Mesozoic and Cenozoic zircons with positive εHf values in the Paleocene-middle Eocene sediments is interpreted by most researchers to indicate major input from the WPA and its proposed continuation in the now subducted or otherwise removed Greater Burma terrane to the north [*Cai et al.*, 2020; *Wang et al.*, 2014; *Zhang et al.*, 2019]. The thickness of Eocene detritus in the CMB [e.g. *Zhang et al.*, 2021] may indicate that the removed component of the Greater Burma terrane was quite substantial. Some samples with a significant component of older grains presumably indicate input from Burmese basement such as the Kampetlets schists and Pang Chaung turbidites. *Arboit et al.* [2021] additionally suggests the possibility of some Himalayan input, delivered by the Bengal Fan / longshore drift.

For formations younger than middle Eocene, provenance is debated. Old zircons and metamorphic lithic fragments in the uppermost middle to lowermost upper Eocene Yaw Formation are considered by *Westerweel et al.* [2020], and *Morley et al.* [2021] to be derived from within the WBT, such as either the Naga metamorphic rocks [*Aitchison et al.*, 2019] or the now-subducted Greater Burma to the north. *Westerweel et al.* [2020] consider that this provenance continues to be dominant in the upper Oligocene Tonhe Formation,

with first input from the MMB in the lower Miocene Letkat Formation. In this scenario, contact between Sibumasu and the WBT is not required until the Miocene. By contrast, *Zhang et al.* [2019] considered that MMB detritus first reached the CMB sometime between the late Eocene and the middle Oligocene, as also proposed by *Arboit et al.* [2021] whilst *Licht et al.* [2018] consider the first appearance of MMB detritus to be in the uppermost middle Eocene to lowermost upper Eocene Yaw Formation, thus requiring contact between Sibumasu and the WBT by the Oligocene and Eocene, respectively.

2.3 Previous work on the exhumation history of the IBR

An early IBR exhumational phase, in the Cretaceous, has been proposed based on the presence of unconformities of that age in the region [e.g. *Brunnschweiler*, 1966; *A H G Mitchell et al.*, 2010], evidence of schist and ophiolitic clasts from the IBR core in Cretaceous IBR sedimentary rocks [e.g. *Morley et al.*, 2020; *Rangin et al.*, 2013], and geochronological dating of rodingites (Liu et al., 2016) and the metamorphic sole of the accretionary prism [*J Zhang et al.*, 2017]. Sedimentological observations, such as the facies change from Cretaceous-Eocene turbidites to imprecisely dated ~upper Eocene to Oligocene (?) continental deposits in the IBR [*Aitchison et al.*, 2019; *Bannert et al.*, 2012; *Ghose et al.*, 2014; *Morley et al.*, 2020] also provide some constraint on the timing of exhumation of the accretionary prism. More precise timings of the exhumation of the IBR have been determined using two approaches: (1) interpretations of the provenance changes in the CMB described above in terms of changing palaeogeography, and (2) low temperature thermochronology age elevation profiles in the IBR.

206 *2.3.1 Changes in the CMB interpreted in terms of exhumation of the IBR.*

207 *Licht et al.* [2018] documented a facies change from delta flood plain to a semi-enclosed
208 barrier setting between the middle Eocene Pondaung Formation and the uppermost middle
209 Eocene to upper Eocene Yaw Formation. They interpreted these changes as due to uplift of
210 the nascent IBR, which formed a barrier. *Arboit et al.* [2021] noted a provenance change at
211 ~39 Ma, which they ascribed to decreasing proportions of Himalayan-derived (arc) material
212 delivered to the CMB from the trench side to the west due to the uplifting IBR acting as a
213 barrier. *Zhang et al.* [2019 and references therein] recorded a change in provenance
214 sometime between late Eocene and middle Oligocene times in the CMB. They interpreted
215 this provenance change to represent a shift from local derivation from the Wuntho-Popa arc
216 to input from the MMB to the north. They concluded that, by this time, the Ayeyawady
217 River must have been in evidence to transport material from the north, requiring an uplifted
218 IBR as its western valley side. However, due to lack of samples over the intervening late
219 Eocene to early Oligocene period, the time of change could not be tied down more
220 precisely.

221

222

223 *2.3.2 Exhumation of the IBR determined from three age elevation profiles, coupled with*
224 *provenance data from east and west of the IBR.*

225 *Najman et al.* [2020] published the only age elevation transect on the IBR, to date. These
226 profiles, in the Mindat region, at the latitude of the paleohigh separating the Minbu and
227 Chindwin sub-basins, showed: (1) a significant period of exhumation around the Oligo-
228 Miocene boundary in the IBR core (19-23 Ma; slightly earlier once advection is taken into

229 account); (2) a period of exhumation to the east in the Kabaw Fault zone at 28-32 Ma (early
230 Oligocene) but with large analytical uncertainties, and (3) tentatively, a possible earlier
231 period of exhumation at or prior to 40 Ma (middle Eocene) in the IBR core, for which further
232 work is required to confirm or refute. In the same paper (*Najman et al.* [2020], the age
233 elevation profile was coupled with provenance data from the adjacent CMB. These data
234 broadly showed (i.e. averaging between sub-basins with different geological histories after
235 they were partitioned from ~39 Ma [*Licht et al.*, 2018]), that until at least the middle Eocene
236 (48-38 Ma), sediment from both east and west of the IBR was derived predominantly from
237 the Wuntho-Popa magmatic arc to the east. This indicates that the IBR had not formed a
238 barrier sufficiently developed to impede westward transport by this time.

239

240 **3. Strategy and methods**

241 As summarised in section 2.2, we [*Zhang et al.*, 2019] previously presented evidence for a
242 change in provenance as occurring definitively sometime after the late middle Eocene and
243 by the middle Oligocene. Therefore, we focussed our new analyses on upper Eocene and
244 lower Oligocene forearc basin sediments to more precisely constrain the time of
245 provenance change, and we also incorporated new data as referenced in the appropriate
246 figure captions.

247 Additionally, our previous work using rutile U-Pb analyses [*Zhang et al.*, 2019] had assumed
248 that grains with Cenozoic U-Pb ages were derived from the MMB. In our current paper, we
249 therefore first undertook rutile analyses from the Ayeyawady headwaters that drain the
250 MMB to confirm this interpretation.

We undertook a second age elevation transect (Tedim transect) to determine how regionally applicable our first transect was [*Najman et al.*, 2020]. Our new transect lies ~200 km north of our previous transect at Mindat (Fig. 1). The location was chosen because it allowed for the collection of multiple steep profiles within fault blocks that are comparable with the previous work. We also undertook additional low temperature thermochronological analyses and modelling of our previous Mindat transect in order to better compare the two transects.

Sample locations are given in SI 1, and detailed methodological descriptions are provided in SI 2, with summaries given below.

3.1 Petrography

450 points were counted on 10 sandstone samples from the CMB using the Gazzi-Dickinson method [*Ingersoll et al.*, 1984]. Sandstone classification was based on the relative abundance of the three main framework components quartz (Q), feldspars (F), and lithic fragments (L), considered if exceeding 10%QFL (e.g., in a litho-feldspatho-quartzose sand Q > F > L > 10%QFL; classification scheme after *Garzanti* [2019]). Full quantitative information was collected on rock fragments, classified according to protolith composition and metamorphic rank [*Garzanti and Vezzoli*, 2003]. Median grain size was determined in thin section by ranking and visual comparison with sieved in-house standards.

3.2 Isotopic analyses

Sr and Nd isotopes on bulk mudstones (six samples from the CMB), together with laser ablation U-Pb analysis of zircon (eight samples, six from the CMB and two from the IBR) and rutile (eight samples, four from the CMB, one from the IBR and three modern river sands), and Hf-isotope analysis of zircon (six samples from the CMB), were carried out at the Geochronology and Tracers Facility, British Geological Survey, UK.

Bulk rock powders were leached in dilute acetic acid to remove carbonate material prior to dissolution. Sr and Nd were separated using AG50x8 and LN Spec resins, and analysed on a Thermo Scientific Triton thermal ionisation mass spectrometer operating in multi-dynamic mode.

U-Pb zircon analyses were carried out using a multicollector Nu Plasma HR mass spectrometer coupled to a New Wave 193SS solid state laser, using the 91500 reference material [*Wiedenbeck et al.*, 1995] as primary reference material. Plešovice zircon [*Sláma et al.*, 2008] and GJ1 [using values recommended by *Horstwood et al.*, 2016] were used as secondary references. Rutile U-Pb analysis was carried out with the same instrumentation using Sugluk [*L. Bracciali et al.*, 2013], R10 [*Luvizotto et al.*, 2009] and R19 [*Zack et al.*, 2011] as reference materials. Rutile ages are corrected for common Pb (see Supplementary file for details). U-Pb data was reduced using Iolite versions 3 and 4 [*Paton et al.*, 2011] and plotted using IsoplotR [*Vermeesch*, 2018]. For grains > 1200 Ma in age, $^{207}Pb/^{206}Pb$ ages were used, with a discordance limit of ± 10%. For grains < 1200 Ma, $^{206}Pb/^{238}U$ ages were used, with a discordance limit of ± 5%.

3.3 Thermochronological analyses

Thermochronologic data were obtained from 17 IBR samples along the road passing through Tedim (Figs. 1, 2A). Five zircon fission track (ZFT) samples were dated at the University of Sao Paulo using the external detector method. Methodology followed *Parra et al.* [2009]. Seventeen zircon and three apatite samples were analyzed using the (U-Th-Sm/He) (ZHe and AHe, respectively) methods at Universitaet Potsdam (alphachron) and GFZ-Potsdam (ICP-MS) following the methodology of *Galetto et al.* [2021] and *Zhou et al.* [2017]. Eleven apatite fission track (AFT) samples were analyzed at the Universitaet Potsdam by ERS using the external detector method following the methods outlined in *Sobel and Strecker* [2003]. Detailed methodological descriptions are provided in SI 2. AFT and ZFT ages are reported with 1 sigma errors (SI 3a, 3c); AHe and ZHe ages are reported with 1 standard deviation errors (SI 3b).

4. Results

4.1 Thermochronologic age patterns determined by QTQt modelling

We obtained thermochronologic ages using up to four methods per sample, with closure temperatures ranging over >170°C [e.g. *Reiners and Brandon*, 2006]. A summary of the data is given in Table 2 and detailed datasets are provides in SI 3a, b and c. All ZFT samples have at least 1 population which is older than the sample depositional age, suggesting that the samples have not been heated significantly within the zircon partial annealing zone (ZPAZ; <~230-350 °C; [*Reiners and Brandon*, 2006]). Therefore, we interpret these ages to represent partially reset (at least 1 population younger than depositional age) or unreset (all populations older than depositional age) detrital ages. Reset ZHe ages are interpreted to

reflect in-situ cooling through the zircon partial retention zone (ZPRZ; 140- ~220 °C; [*Guenthner et al.*, 2013]); partially reset samples only attained temperatures in the lower part of this range. All AFT ages are much younger than depositional age and therefore are interpreted to reflect relatively rapid cooling through the apatite closure temperature of ~120°C within the past ~10 Ma [e.g. *Reiners and Brandon*, 2006]. All AHe ages are interpreted to reflect relatively rapid cooling through the apatite partial retention zone (APRZ; 40-~80 °C [e.g. *Reiners and Brandon*, 2006]). We performed inverse modelling with the QTQt program (v. 5.7.0), which uses a Bayesian transdimensional statistical approach to extract the most probable thermal history from robust datasets [*Gallagher*, 2012]. Detailed descriptions of the modeling strategy and of each model are provided in SI 4; supporting figures are shown in SI 5.

4.1.1. Tedim transect

The thermochronologic ages and sample elevations are plotted versus position along the Tedim cross-section within a topographic swath profile and on a geological map (Fig. 2). We divided the Tedim cross-section into five fault-bounded segments, named zones T1 to T5, from west to east. These blocks are separated by the Lemyo, Thoubal, Zunki and Kheng faults (Mitchell 2018; Singh, 2016; Morley et al., 2020). The Lemyo Fault may be correlated with the Lelon Fault (Mitchell 2018). In order to assess the thermochronologic data from each fault block together, we performed inverse modeling of each Tedim zone (Fig. 3).

4.1.1.1 Zone T5 (Kheng transpressive shear zone)

340 The three modelled samples from zone T5 (MY19-87a, -88a, -89a) were near the surface at a
341 time corresponding to a late Triassic - early Jurassic depositional age [*Yao et al.*, 2017]. They
342 were again near the surface between 127 and 115 Ma, when ophiolites were formed and
343 emplaced (Liu et al., 2016). Subsequently, samples were heated by burial beneath
344 sediments prior to final Cenozoic exhumation. Sample MY18-86a was not modeled due to
345 ambiguity about its position with respect to the Kheng fault. The modeled ZHe samples all
346 have significant age dispersion, which cannot be simply related to either eU or grain size (SI
347 5a). The likely explanation for the large ZHe age dispersal is variable inherited radiation
348 damage; the zircons in this section have U/Pb ages ranging from 187 Ma to ~1200 Ma and
349 older (Yao et al., 2017). An alternative possibility is that the ZHe crystals are not fully reset.

350 We tried two modeling strategies (SI 4a). First, we modeled all ZHe aliquots; this led to
351 geologically unrealistic results and poor fits to the individual aliquots (Fig. SI 5c). We also
352 modeled just the younger ZHe aliquots on the logic that it is more common for older ages to
353 be erroneous. (Fig. SI 5c). However, comparing these two models, the onset of rapid cooling
354 is clearly dependent on the choice of aliquots modeled and one could easily obtain different
355 model results by selecting a different aliquot (SI 4a). Therefore, we refrain from using the
356 model results from this zone.

357

358 *4.1.1.2 Zone T4 (Kheng fault to Zunki fault).*

359 The thermal model (Fig. 3a) shows monotonic heating from late Cretaceous deposition
360 (Mitchell et al., 2010) (Fig. 2) to Tmax of ~180-200°C at ~24-22 Ma followed by monotonic
361 rapid cooling starting around 22 Ma (24-21 Ma).

362

363 *4.1.1.3 Zone T3 (between Zunki and Thoubal faults)*

364 The thermal model (Fig. 3c) shows monotonic heating from the 45-49 Ma depositional age
365 based on the MDA from sample MY18-78A determined from detrital zircon U-Pb data (SI
366 3d), to a Tmax of ~180-260°C at ~25 Ma, followed immediately by 5-10 Myrs of rapid
367 cooling. There is a possible reheating interval between ~18-10 Ma, then renewed rapid
368 cooling beginning at ~10 Ma. The apparent reheating could reflect a combination of a
369 decrease in exhumation rate and advection rather than burial.

370

371 *4.1.1.4 Zone T2 (Thoubal Fault to Lemyo west-vergent Fault)*

372 The thermal model (Fig. 3e) shows monotonic heating from the ~50 Ma depositional age
373 based on the youngest detrital zircon U-Pb age in MY18-74A (SI 3d), to a Tmax of ~170-300
374 °C at ~21 Ma, followed immediately by rapid monotonic cooling. The cooling rate decreases
375 between ~9 - ~3 Ma before increasing again.

376

377 *4.1.1.5 Zone T1 (west of Lemyo west-vergent thrust)*

378 Samples from Zone T1 were collected from the Eocene - Oligocene Barail Group [*Handique*
379 *et al.*, 1989] near the Indian border (Fig. 2). The depositional age is constrained by sample
380 MY19-169A, which has one discordant U/Pb zircon at ~40 Ma as well as three detrital rutiles
381 between ~41 Ma and 37.5 Ma (SI 3d and e). The same sample yielded three ZHe ages:
382 33.4±0.6, 35.8±0.4, and 41.6±0.5 Ma. Zone T1 has a younger depositional age and a more
383 distal position than zone T2 and therefore would be expected to have lower maximum
384 burial temperature but a generally similar pattern of burial heating. Therefore, we interpret

385 the zircon crystals to represent roughly syn-depositional volcanic grains which have only
386 experienced enough burial to reset the AFT age of sample MY19-170A (Fig. 3g).
387 Alternatively, the ZHe ages could reflect Himalayan-derived detrital material, similar to
388 results from sample 16CMP7, collected 25 km to the NW from the middle Barail Group [*P.M.*
389 *Betka et al.*, 2021]; this scenario would require a similar magnitude of burial heating over a
390 shorter interval. The thermal model shows a poorly constrained cooling path close to the
391 deposition age, which is set to 32-30 Ma. The model then shows slow heating between ~25
392 Ma and 15-10 Ma, followed by slow cooling beginning at ~13-10 Ma. Maximum burial
393 temperatures were 80-120°C.

394

395 *4.1.2. Mindat transect*

396 We modeled the cooling history of two of the three blocks from the Mindat transect using
397 new ZHe data and data presented in *Najman et al.* [2020] in order to strengthen the
398 conclusions of that study (Fig. 4).

399

400 *4.1.2.1 Mindat IBR core*

401 The Mindat IBR core profile includes data from 4 samples: 1 unreset or partially reset ZFT
402 age, 3 ZHe samples with a total of 11 reproducible aliquots, and 3 AFT samples (Fig. 4b).
403 Here, we neglect three younger ZFT crystals that have too much age dispersion to define a
404 single population. The new ZHe data from sample MY16-17A is reported in Table 2 and SI
405 3b. In addition, sample MY16-35a likely belongs to this profile. As this sample has one low
406 resolution AFT age, two discordant ZHe ages, and a partially reset ZFT age, it was not
407 included in the thermal model. Recent mapping suggests that the Kanpetlet schist is

bounded to the east by an unconformity (Morley et al., 2020) rather than by the Kabaw fault, as portrayed in Najman et al. (2020); therefore, we have modified the cross-section shown in Fig. 4b. The model (Fig. 4c) shows that the profile was near the surface at the Triassic depositional age (Yao et al., 2017) and again around ~128-115 Ma, when ophiolites were formed and emplaced (Zhang et al., 2017a). Subsequently, samples were heated by burial beneath sediments until ~57-49 Ma and ~200-240°C. Monotonic cooling commenced at ~49±3 Ma and continued until the present. This fault block is correlated with zone T5 of the Tedim profile.

4.1.2.2 West of and within the Lelon fault zone

The QTQt model for the western end of the Mindat profile (west and within Lelon fault zone; Fig. 4b, f) includes data from 5 samples: 1 partially reset ZFT age, 4 ZHe samples with a total of 23 aliquots (of which 5 were discarded), and 2 AFT samples. The new ZHe data from sample MY16-32A are reported in Table 2 and SI 3b; the remaining data are from *Najman et al.* [2020]. The ZHe data generally show a good age-elevation trend (Fig. 4f). The thermal model shows a complex pattern, with rapid post-depositional heating to 310-150°C at ~30 Ma, followed by a pulse of cooling until 27-22 Ma, then reheating until ~19 Ma, and finally monotonic cooling. The apparent reheating could reflect a combination of a decrease in exhumation rate and advection rather than burial.

4.1.3. Summary of thermochronologic results

In zones T2, T3, and T4 of the Tedim profile, and the Mindat IBR core, ZHe ages young westward within each block. Not all of the ages are correlated with elevation. Two of the

three samples in Zone T5 of the Tedim profile also follow this pattern. In addition, the QTQt models show a very small thermal offset between the lowest (hot) and highest (cold) samples. However, the elevation offset between the samples would suggest a larger thermal offset. This pattern could be explained by rotation of the blocks about a horizontal axis trending subparallel with the bounding fault systems. This may be caused by west-vergent thrusting on the western-margins of the fault blocks or possibly by deformation within the individual blocks.

Our QTQt modeling shows that most of the range covered by our transects has experienced over 160°C of Cenozoic exhumation. The core of the range, exposing Triassic strata and metamorphic rocks, commenced a period of exhumation in the early-middle Eocene. This is slightly earlier than the poorly dated change from deep marine to continental facies between the middle and late Eocene in the IBR (c.f. sections 2.1.2 and 2.3). The bulk of the exhumation initiated in the latest Oligocene and propagated westward. The AFT ages are quite consistent across much of the range, with most ages between 6-9 Ma, irrespective of elevation. This could suggest that the range has reached an exhumational steady state (e.g., Reiners and Brandon, 2006). In contrast, AFT ages in the far western region are slightly older (6-11 Ma), reflecting the slower exhumation in this block (Fig. 3).

4.2 Provenance data:

In summarising the salient points of our results, we put them in context of previously published results.

4.2.1 Petrography

454 The analysed samples (reported in dataset SI 3g and graphically presented in Fig. SI 6) range
455 from very-fine to medium sand (4.0 to 1.4 ϕ). The majority of samples of late Eocene
456 (Chindwin Basin) or Early Oligocene (Minbu Basin) ages and younger are litho-feldspatho-
457 quartzose. Samples older than late Eocene have more feldspar and/or lithic fragments in
458 both basins. An evolutionary trend from the middle Eocene to the Miocene is documented
459 by increasing sedimentary and metamorphic lithic fragments, at the expense of volcanic
460 lithic fragments. Petrography is stable from Miocene onwards.

461 In the Chindwin Basin, the feldspar-rich middle Eocene Pondaung Formation indicates
462 predominant derivation from the roots of a magmatic arc. The major influx of metamorphic
463 detritus is indicated by biotite and staurolite in the lower Miocene Letkat Formation,
464 indicating supply from amphibolite-facies metasedimentary rocks. The underlying latest
465 middle to lowermost upper Eocene Yaw Formation is transitional between the Pondaung
466 and Letkat formations. Oligocene rocks were not sampled in the Chindwin Basin. The onset
467 of metamorphic detritus is more difficult to pin-point in the Minbu basin. Eocene to Lower
468 Oligocene sandstones of the Pondaung and Shwezetaw Formations are volcaniclastic and
469 chiefly arc- derived. The most significant petrographic change is marked by decreasing
470 plagioclase and volcanic detritus, which are largely arc-derived, with a relative increase in
471 quartz, K-feldspar and amphibole. This provenance change occurs between the lower
472 Oligocene Shwezetaw Formation and the upper Oligocene Okhmintaung Formation, with
473 the occurrence of amphibole at this time suggesting input from amphibolite-facies
474 metamorphic rocks rather than the arc [*Andò et al.*, 2014]. Biotite becomes abundant and
475 staurolite common in lower Miocene sandstones which also contain garnet, whilst kyanite is
476 first recorded in the Irrawaddy Formation above. This indicates that supply from
477 amphibolite-facies metamorphic rocks continued throughout the Neogene.

478

479 *4.2.2 Zircon U-Pb with Hf (dataset SI 3d)*

480 As illustrated in Fig 5, previous data from all CMB sub-basins studied (Chindwin and
481 backarc/on-arc) show that for all formations up to and including middle Eocene strata, the
482 <250 Ma zircon population has almost exclusively positive εHf values [*Arboit et al.*, 2021; *Lin*
483 *et al.*, 2019; *Wang et al.*, 2014; *Zhang et al.*, 2019]. We now show that this is also true for
484 the Minbu Basin (sample MY16-05A, Middle Eocene).

485 No previously published data are available for the latest middle to lowermost upper Eocene
486 Yaw Formation. The only available data were from the upper Eocene backarc sediments
487 [*Zhang et al.*, 2019], which show a predominance of grains with positive εHf values for
488 grains < 250 Ma, but with low number of analyses. Our new data from the Yaw Formation
489 (MY18-95A) shows that Mesozoic-Cenozoic zircons with negative εHf values remained rare
490 in the CMB during this time interval.

491 Above the Eocene, there was previously no published data from the forearc strata until the
492 Miocene [*Arboit et al.*, 2021; *Wang et al.*, 2014; *Zhang et al.*, 2019], where detrital zircons in
493 the <250 Ma age range have an appreciable proportion of grains with negative εHf values.
494 Our new data from the Minbu forearc sub-basin shows that all <250 Ma zircons have
495 positive εHf values in the Lower Oligocene sample (MY16-06A). Grains with negative εHf
496 values first appear in this basin in the Late Oligocene. This is similar to published data from
497 the backarc / on-arc succession that showed the first significant input of zircons with
498 negative εHf values in middle Oligocene strata [*Arboit et al.*, 2021; *Robinson et al.*, 2014]. In
499 all basins studied, the proportion of grains with such a signature progressively increase into
500 the Neogene.

501

502 *4.2.3 Rutile U-Pb (dataset SI 3e)*

503 As illustrated in Fig 6, previously published data from all studied CMB sub-basins [Chindwin,
504 Minbu and back-arc/on-arc; *Arboit et al.*, 2021; *Zhang et al.*, 2019] show that formations up
505 to and including the latest middle to lowermost upper Eocene Yaw Formation either have
506 grain age spectra composed exclusively of ~500 Ma and/or ~100 Ma peaks, with no
507 Cenozoic grains, or samples contain no rutile. Cenozoic grains have been recorded from
508 middle Oligocene (on arc/back arc basin) and lower Miocene strata (Chindwin basin) and in
509 these two basins no rocks from the intervening Eocene-Oligocene time periods have been
510 available for study. Our new data from the Minbu Basin and modern Ayeyawady
511 headwaters allow a more complete representation of the trend. The middle Eocene sample
512 contains no rutile (MY16-05A) consistent with previous studies of this time period; the lower
513 Oligocene sample (MY16-06A) contains a small Cenozoic population which increases in
514 dominance and youngest grains in the upper Oligocene sample (MY16-11A). This trend of
515 increasing dominance of Cenozoic grains continues throughout the Neogene, also more
516 clearly observed in our new data from Neogene samples including from the Chindwin Basin
517 (MY16-10A – Lower Miocene, MY16 09A and 56A – middle Miocene-Pliocene).The present
518 day modern Ayeyawady sands (Upper Ayeyawady River; samples MD297, 298, 393) have
519 somewhat lower percentages of Cenozoic grains compared to the Neogene strata.

520

521 *4.2.4 Sr-Nd bulk rock (dataset SI 3f)*

522 Sr-Nd bulk data has previously been used in the CMB to assess the varying contributions of
523 arc versus older continental crustal material through time. Utilising data from both

sandstone and mudstone, and reporting εNd values only, *Licht et al.* [2014] noted a trend to increasingly negative (crustal) values in the Minbu forearc basin from the start of their studied record in the middle Eocene Tabyin Formation, with values becoming stable by the Miocene. Later, *Zhang et al.* [2019] utilised paired $^{87}Sr/^{86}Sr$ and εNd values, and combined both the data from *Licht et al.* [2013] with their additional data from the Minbu forearc basin, as well as reporting the first data from the backarc.

We augment data summarised above from the forearc basin by adding new data from the Chindwin sub-basin, and additionally plotting the data of *Licht et al.* [2013] and *Licht et al.* [2014] as individual points. Note that we only plot their bulk mudstone or <2 micron fraction samples because their data shows appreciable difference between >163 and <2 micron grain-size fractions. The resulting Fig SI 7a shows the trend to increasing proportions of old continental crustal material through time as originally proposed by *Licht et al.* [2014]. This trend begins at least by the middle Eocene, and there is no step change in the Yaw Formation, or discernible difference between the Yaw Formation and underlying middle Eocene Pondaung Formation. In the backarc basin, the data of *Zhang et al.* [2019] record increasing input of older continental crustal material beginning sometime after the middle or late Eocene and before the late Oligocene. We added a sample from the middle Oligocene (Fig SI 7b) and showed that the trend to increasing older continental crustal material had begun by this time.

5. Discussion

5.1 Provenance

As summarised in section 2.2, different published provenance datasets have variously indicated a continuum of change since at least the middle Eocene [*Licht et al.*, 2014], or a step change either in the uppermost middle to lowermost upper Eocene Yaw Formation [*Licht et al.*, 2018], sometime between the late Eocene and early Oligocene [*Zhang et al.*, 2019], or across both the middle Eocene-early Oligocene and Oligo-Miocene boundaries [*Westerweel et al.*, 2020]. Furthermore, the source of the detritus is also debated, with MMB material considered to have first arrived on the WBT either at the middle-late Eocene boundary as detected in the Yaw Formation [*Licht et al.*, 2018], sometime between the late Eocene and middle Oligocene [*Zhang et al.*, 2019], Oligocene [*Arboit et al.*, 2021; *Zhang et al.*, 2021], or Miocene [*Westerweel et al.*, 2020]. The timing of these provenance changes constrains when the WBT docked with Asian Sibumasu.

We are not confident that the Yaw Formation documents an abrupt change in provenance as argued by *Licht et al.* [2018], based on the first appearance of old zircon grains, because such grains have already appeared sporadically but in appreciable numbers in older strata (Fig. SI 8 – zircon U-Pb KDEs), as indeed noted by those authors as evidence of ephemeral earlier exhumation. Likewise, it should be noted that the petrographic change reported at the Pondaung-Yaw Formation boundary in the Chindwin Basin, with increasing metamorphic lithic fragments at the expense of volcanic lithics, also reflects a change in operator (data obtained by *Wang et al.* [2014] for the Pondaung Formation versus data obtained by *Licht et al.* [2018] for the younger units). Petrographic data is sensitive to operator nuances, and in fact, when looking at the data collected by one operator only [*Licht et al.*, 2018] their one datapoint for the “pre Yaw unit” (Paunggyi Fm) is similar to that of their Yaw data, with the main change occurring between the Yaw and the Letkat formations. This is similar to what we observe in our new dataset (Fig SI 6), with the most significant change on an overall

evolution from middle Eocene to Miocene times occurring at the latest Oligocene to Miocene times. Furthermore, Yaw Formation zircon Hf values (Fig. 5) and Sr-Nd signatures (Fig. SI 7) remain similar to those of the underlying Pondaung Formation.

Regardless of whether a change occurred in the Yaw Formation, the important issue is whether the non-volcanic material reflects input from the MMB and therefore whether WBT-Sibumasu collision had occurred by that time. As previously proposed by *Westerweel et al.* [2020] and *Morley et al.* [2021], old zircons and metamorphic rock fragments may reflect greater contribution from Burmese basement where, for example, Triassic schists show a significant pre-Devonian zircon population [*Najman et al.*, 2020; *Sevastjanova et al.*, 2015; *Yao et al.*, 2017], and/or from the now-subducted Greater Burma region or Naga metamorphic rocks of the WBT. To this discussion, we bring the first zircon εHf data from the Yaw Formation, which shows a paucity of grains with negative values, indicating an absence of zircons from the MMB. We therefore concur with those previous workers who propose a source within the WBT for the non-volcanic detritus deposited in the Yaw Formation of the CMB in latest middle to earliest late Eocene times.

Arboit et al. [2021] also note a change in provenance in the middle to late Eocene. They tentatively ascribe this provenance to Bengal Fan Himalayan detritus, delivered to the CMB from the west, with decreasing Himalayan input again from 39 Ma due to the uplifting IBR acting as a barrier. Their argument for a new Himalayan provenance in the middle-late Eocene can be summarised as: samples include Neoproterozoic-Cambrian zircons with Hf values as low as -50 which they suggest have not been so far recorded in the WBT; zircon Hf values of the Mesozoic-Cenozoic grains become more heterogenous compared to underlying formations; and apatite and titanite grains dated 110-85 Ma have geochemical

compositions indicative of derivation from high grade metamorphic rocks suggested to be from the Lhasa terrane north of the Himalayan Yarlung-Tsangpo suture zone. We provide the following counter-arguments: 1) the Pane Chaung Formation (Triassic turbidites of the IBR, thought to represent the unmetamorphosed equivalent of the Kanpetlet Schist of the Burmese basement [*Bannert et al.*, 2012; *Morley et al.*, 2020]) contain zircons of suitable age and εHf affinity [*Yao et al.*, 2017]; 2) εHf values do not become significantly more heterogenous; there is only one Mesozoic-Cenozoic zircon with negative εHf value, all others being of positive signature compatible with a WPA source; 3) the, albeit limited, studies of titanite from the Lhasa Block all have ages <100 Ma and the majority <85 Ma [*Guo et al.*, 2020]; 4) a Himalayan suture zone high-grade metamorphic source delivered to the CMB via the Bengal Remnant Ocean Basin and the Indian Ocean represents a palaeodrainage pattern not easily envisioned both in terms of i) the depositional patterns that would be required, and ii) the lack of high-grade metamorphic charnokite material recorded in petrographic data from late Eocene rocks of the Bengal (Surma) Basin [*Najman et al.*, 2008]; metamorphic minerals are not recorded in the Surma Basin until post-Eocene times [*Laura Bracciali et al.*, 2015].

Zhang et al. [2019] previously proposed a change in provenance sometime between the late Eocene and middle Oligocene. They noted the first appearance of zircons with negative εHf values typical of the MMB and Cenozoic rutiles which they interpreted as MMB-derived, by the middle Oligocene. With our new data that better spans the missing time interval, we now refine the change as occurring after the latest middle to lowermost upper Eocene Yaw Formation [depositional age ~39-37.8 Ma *Licht et al.*, 2018], as evidenced by the Mesozoic-Cenozoic zircons with positive εHf values, and by the early Oligocene, as evidenced by first appearance of Cenozoic rutile at this time. First input of MMB-derived material from the

618 Asian plate in the later late Eocene or by the early Oligocene at latest, is coeval with the
619 unconformity above the Yaw Formation, interpreted as due to collision of the WBT with Asia
620 [*Westerweel et al.*, 2020]. Our interpretation of first MMB input by the Oligocene rather
621 than Miocene provides stronger support for their hypothesis. The lack of unconformity in
622 the forearc basin further south (Minbu Basin) may reflect the decreasing influence of
623 collision in more southern distal settings.

624 The influence of the MMB then increased through time throughout the Oligo-Miocene, as
625 evidenced by the increased proportion of metamorphic detritus, young zircons with
626 negative εHf values and Cenozoic rutiles, and Sr-Nd signatures moving towards a higher
627 proportion of old crustal material. This is consistent with the timing of exhumation of the
628 MMB (section 2.1). This gradual evolution of provenance with increase in the proportion of
629 MMB through time since the Oligocene is at variance with the proposal of *Westerweel et al.*
630 [2019]. Those authors considered that MMB detritus first arrived on the WBT in the
631 Miocene, above an unconformity between the Tonhe and Letkat formations, with both the
632 unconformity and provenance change explained as due to indentation of the WBT into the
633 eastern Himalayan syntaxis. With our alternative view, this then leaves a question over the
634 cause of the unconformity in the Central Myanmar Basins at the Oligo-Miocene boundary.
635 We note that this time is coeval with a period of exhumation in the IBR (Najman et al 2020,
636 this paper section 4.1.3) for which there may be a common cause.

637

638 ***5.2. Age elevation profiles***

639

640 *5.2.1 Tedim age elevation transect*

The time when the IBR core in the Tedim section (Zone T5) began to be exhumed is poorly constrained but appears to be older than the zones farther west. Zones T2, T3 and T4 were all heated beneath accumulating strata during the Eocene. Our thermal models do not have the resolution to detect small duration and short magnitude exhumation pulses during this time; however, all three zones were heated from deposition to over 170°C in this interval. The main phase of rapid exhumation occurred during the latest Oligocene - early Miocene. Rapid cooling starting in zone T3 around 25 Ma (~26-20 Ma). Very rapid cooling starts in zone T2 at ~20 Ma and in zone T1 at ~10 Ma. Therefore, deformation propagated generally westward from zone T4 to T1. The similar magnitude of exhumation in the first three of these four blocks suggests that the intervening Zunki and Thoubal faults have limited vertical offsets. However, as zone T1 began to be exhumed more recently, we suggest that the Lemyo Fault must have been the most important structure controlling Oligo-Miocene shortening.

5.2.2. Refining the Mindat Age Elevation Transect of Najman et al. [2020].

We correlate Zone T5 of the Tedim profile with the Kanpetlet schist-bearing IBR core in the Mindat profile, where exhumation commenced at ~49 ± 3 Ma (Figs. 2, 4c). The onset of exhumation proposed in Najman et al. (2020) for the Mindat section, at or prior to 40 Ma, was estimated using age-elevation pseudovertical profiles. These profiles did not include ZFT data because it is hard to assign a precise closure temperature to ZFT data. In contrast, the QTQt models incorporate the ZFT data by limiting the temperature range that the model examines, and uses radiation damage-constrained ZHe models, as well as the depositional ages of the samples. Therefore, they provide loose constraints on the heating paths and

better define the inflection point delineating the transition from burial to exhumation. Our QTQt model of the Mindat IBR core (Fig. 4c, d), now incorporating this additional information, confirms the Eocene pulse of cooling and refines the onset age to ~49 ± 3 Ma.

5.2.3 Discussion on age elevation profile data.

In both our previously published and new age elevation profiles, a major period of exhumation occurs at the time of the Oligo-Miocene boundary. Previously we suggested that the cause of this exhumation episode may have been a change in wedge dynamics associated with increased sedimentation to the system from the Bengal Fan [*Najman et al.*, 2020]. Additionally, our new data from the Mindat profile strengthen our Tedim dataset, indicating another period of exhumation of the IBR in the early-middle Eocene, now dated around ~49 ± 3 Ma. Exhumation at both sections was likely controlled by the west-vergent Kheng fault, west of the IBR core. This exhumation event may be related to the timing of collision between the WBT and India, as constrained by palaeomagnetic data, considered by *Westerweel et al.* [2019] to show collision around 40 Ma, with later refinement [*Westerweel*, 2020 quoted in Morley et al. (2021), their Fig 3D] indicating collision may be as old as 50 Ma. However, for both Oligo-Miocene and Eocene events, other previously proposed mechanisms remain equally valid, for example a change in angle of the subducting slab, the influence of the prism's location in a hyper-oblique setting with localised strain partitioning, changes in plate kinematics, impact of the 90E Ridge, or collision of the WBT with a small allochthonous terrane or island arc (see reviews in *Licht et al.* [2018] and in *Morley and Arboit* [2019], and papers by *Acharyya* [2015], *Maurin and Rangin* [2009], and [*S H Li et al.*, 2018]).

6. Conclusions

Our provenance data from the Central Myanmar Basins indicate that detritus from the Mogok Metamorphic Belt and spatially associated granites was first deposited in the CMB of the West Burma Terrane after the early part of the late Eocene and by the early Oligocene, based on a lack of such material in the earliest upper Eocene rocks and its presence in lower Oligocene strata. These results provide a minimum age constraint to the timing of WBT-Asia collision, which may also be responsible for the unconformity observed in the CMB at this time. We interpret that any potential earlier provenance change was related to influx from basement material within the WBT rather than influx from the MMB.

Our low temperature thermochronology data from the IBR record periods of exhumation in the early-middle Eocene and around the Oligo-Miocene boundary. The early-middle Eocene period of exhumation may be associated with the collision of WBT with India. In *Najman et al.* [2020] we proposed that the major period of exhumation at the Oligo-Miocene boundary may be related to a change in wedge dynamics associated with increased sedimentation to the system from the Bengal Fan. However, we note that for both the Eocene and Oligo-Miocene events, a number of other viable proposed mechanisms remain.

Acknowledgements

We thank the guides and drivers in Myanmar for enabling the field work, and technical staff at NIGL for analytical support. Discussions with Alexis Licht (CNRS, Aix-en-Provence, France), Chris Morley (Chiang Mai University, Thailand), Shihu Li (Chinese Academy of Sciences, Beijing), Pierrick Roperch and Jan Westerweel (University of Rennes) helped clarify our ideas. Constructive reviews from Alexis Licht, Pierrick Roperch and an anonymous reviewer improved the quality of this submission. Data is accessible in supporting information for review purposes and will be made available on figshare at 10.6084/m9.figshare.17283962 upon acceptance. This work is supported by National Natural Science Foundation of China (No. 92055211), China-ASEAN Maritime Cooperation Fund Project (No. 12120100500017001).

FIGURES

Fig 1. Geological map of Myanmar, also showing study areas of the age elevation profiles (Figs 2 and 4). Map is adapted from *A H G Mitchell et al.* [2012] and *Robinson et al.* [2014], and references therein.

Fig. 2 Tedim transect thermochronologic data displayed on a geologic map (A) and cross-section. Geological map modified from *Burma Earth Sciences Research Division* [1977], *A Mitchell* [2018], *Morley et al.* [2020], and Singh (2016). Blue rectangle delineates footprint of topographic swath profile used to calculate minimum, mean and maximum elevations shown in B. B) Age (left axis) and elevation (right axis) of thermochronologic samples projected onto an east-west profile. Positions are shown with respect to the westernmost

730 sample, MY19-169. Prefix MY- has been removed from sample numbers for clarity. Detrital
731 zircon data in zone T5 is from Yao et al. (2017).

732 **Fig. 3.** Tedim QTQt model results for zones T4 through T1. Left column (a, c, e, g,) shows the
733 expected thermal history models. The red curves denote the “hot sample” and the dark blue
734 curves the “cold sample” with their respective 95% confidence intervals. Heavy green boxes
735 indicate the depositional age constraints. Red box delineates the model space. Right column
736 (b, d, f, h) shows how well the model fits the observed data; key is in panel b. We present
737 the values predicted for the expected thermal history model and the 2-sigma interval of the
738 data predicted by the post-burn-in acceptable models. For samples with multiple ZHe or
739 AHe ages, a small elevation perturbation was added to the plot to facilitate data
740 visualization. The predicted ages are connected by dashed lines. Note that the model fits
741 shows AHe and ZHe Ft uncorrected ages. LL is Log-likelihood. Model results for zone T5 are
742 shown in SI 5c.

743 **Fig. 4.** Mindat transect thermochronologic data. A) Swath profile showing minimum, mean
744 and maximum elevations and sample locations. B). Thermochronologic ages and detrital
745 zircon maximum depositional ages projected onto an east-west profile. Sample numbers are
746 shown without prefix MY16- for clarity. A and B are slightly modified from *Najman et al.*
747 [2020]; this reference also provides a geological map of the transect. C, E) QTQt expected
748 thermal history models of the IBR core and the area west and within the Lelon fault zone,
749 respectively. D, F) Model fits to the observed data. Figure explanations and the symbols
750 used are the same as in Fig. 3.

751

Fig 5. Zircon U-Pb with Hf data. Pie charts show the proportion of the <250 Ma zircon population which have positive (black) versus negative (white) εHf values. Samples marked with * are our new data. Published data: 1-*Wang et al.* [2014]; 2-*Arboit et al.* [2021]; 3-*Zhang et al.* [2019]; 4-*Liang et al.* [2008]; 5- *Robinson et al.* [2014]; 6- *Lin et al.* [2019]. Panel D taken from *Zhang et al.* [2019 and references therein], updated with data from *Gardiner et al.* [2018], *J-X Li et al.* [2019], *J-X Li et al.* [2020], *Lin et al.* [2019] and *Zhao et al.* [2017].

Fig 6. Rutile U-Pb data. our new data are marked by asterisks, while the published samples are shown by numbers: 1- *Zhang et al.* [2019] and 2- *Arboit et al.* [2021].

Tables:

Table 1: Summary of Central Myanmar Basins stratigraphy. Information taken from *Licht et al.* [2013], [*Licht et al.*, 2018], *Arboit et al.* [2021], *Bender* [1983], *Htut* [2017], and *Zhang et al.* [2019] and references therein.

Table 2: Thermochronologic data summary

References

Acharyya, S. K. (2015), Indo-Burma Range: a belt of accreted microcontinents, ophiolites and Mesozoic-Paleogene flyschoid sediments, *International Journal of Earth Sciences*, *104*(5), 1235-1251.

Aitchison, J. C., J. R. Ali, and A. M. Davis (2007), When and where did India and Asia collide?, *Journal of Geophysical Research*, *112*, B05423, doi:05410.01029/02006JB004706,.

Aitchison, J. C., et al. (2019), Tectonic Evolution of the Western Margin of the Burma Microplate Based on New Fossil and Radiometric Age Constraints, *Tectonics*, *38*(5), 1718-1741.

Andò, S., A. Morton, and E. Garzanti (2014), Metamorphic grade of source rocks revealed by chemical fingerprints of detrital amphibole and garnet, in *Sediment provenance studies in*

hydrocarbon exploration and production, edited by R. A. Scott, S. H.R., A. C. Morton and N. Richardson, pp. 351-371, Geological Society London, Special Publication.
Arboit, F., M. Min, D. Chew, A. Mitchell, K. Drost, E. Badenszki, and J. S. Daly (2021), Constraining the links between the Himalayan belt and the Central Myanmar Basins during the Cenozoic: An integrated multi-proxy detrital geochronology and trace-element geochemistry study, *Geoscience Frontiers*, *12*(2), 657-676.
Bannert, D., A. Sang Lyen, and T. Htay (2012), *The geology of the Indoburman Ranges in Myanmar*, Geologisches Jahrbuch.
Barber, A. J., K. Zaw, and M. J. Crow (2017), The pre-Cenozoic tectonic evolution of Myanmar, in *Myanmar; Geology, Resources and Tectonics*, edited by A. J. Barber, K. Zaw and M. J. Crow, pp. 687-712, Geological Society of London, Memoirs.
Barley, M. E., A. L. Pickard, K. Zaw, P. Rak, and M. G. Doyle (2003), Jurassic to Miocene magmatism and metamorphism in the Mogok metamorphic belt and the India-Eurasia collision in Myanmar, *Tectonics*, *22*(3).
Bender, F. (1983), *Geology of Burma*, Borntraeger, Berlin.
Bertrand, G., C. Rangin, H. Maluski, and H. Bellon (2001), Diachronous cooling along the Mogok Metamorphic Belt (Shan scarp, Myanmar): the trace of the northward migration of the Indian syntaxis, *Journal of Asian Earth Sciences*, *19*(5), 649-659.
Betka, P. M., L. Seeber, S. N. Thomson, M. S. Steckler, R. Sincavage, and C. Zoramthara (2018), Slip-partitioning above a shallow, weak decollement beneath the Indo-Burman accretionary prism, *Earth and Planetary Science Letters*, *503*, 17-28.
Betka, P. M., S. N. Thomson, R. Sincavage, C. Zoramthara, C. Lalremruatfela, K. A. Lang, M. S. Steckler, D. Bezbaruah, P. Borgohain, and L. Seeber (2021), Provenance shifts during Neogene Brahmaputra Delta progradation tied to coupled climate and tectonic change in the Eastern Himalaya, *Geochemistry Geophysics Geosystems*, *22*, e2021GC010026. https://doi.

org/010010.011029/012021GC010026.
Bracciali, L., R. Parrish, M. Horstwood, D. Condon, and Y. Najman (2013), U-Pb LA-(MC)-ICP-MS dating of rutile: New reference materials and applications to sedimentary provenance, *Chemical Geology*, *347*, 82-101.
Bracciali, L., Y. Najman, R. R. Parrish, S. H. Akhter, and I. Millar (2015), The Brahmaputra tale of tectonics and erosion: Early Miocene river capture in the Eastern Himalaya, *Earth and Planetary Science Letters*, *415*, 25-37.
Brunnschweiler, R. O. (1966), On the geology of the Indoburman ranges, *Journal of the Geological Society, Australia.*, *13*, 137-194.
Burma Earth Sciences Research Division, B. (1977), Geological map of the Socialist Republic of the Union of Burma, 1:1000000, Security Printing Works, Burma, Burma.
Cai, F. L., L. Ding, Q. H. Zhang, D. A. Orme, H. H. Wei, J. X. Li, J. E. Zhang, T. Zaw, and K. Sein (2020), Initiation and evolution of forearc basins in the Central Myanmar Depression, *Geological Society of America Bulletin*, *132*(5-6), 1066-1082.
Galetto, A. V., et al. (2021), Cretaceous and Eocene rapid cooling phases in the Southern Andes (36°-37°S): Insights from low-temperature thermochronology, U-Pb geochronology, and inverse thermal modeling from Domuyo area, Argentina., *Tectonics*, *40, https://doi.org/10.1029/2020TC006415*.
Gallagher, K. (2012), Transdimensional inverse thermal history modeling for quantitative thermochronology, *Journal of Geophysical Research*, *117*, B02408, doi:02410.01029/02011JB008825.
Gardiner, N. J., M. P. Searle, C. K. Morley, L. J. Robb, M. J. Whitehouse, N. M. W. Roberts, C. L. Kirkland, and C. J. Spencer (2018), The crustal architecture of Myanmar imaged through zircon U-Pb, Lu-Hf and O isotopes: Tectonic and metallogenic implications, *Gondwana Research*, *62*, 27-60.
Garzanti, E. (2019), Petrographic classification of sand and sandstone, *Earth Science Reviews*, *190*, https://doi.org/10.1016/j.earscirev.2018.1012.1014.

828 Garzanti, E., and G. Vezzoli (2003), A classification of metamorphic grade in sands based on their
829 composition and grade., *Journal of Sedimentary Research*, *73*, 830-837.
830 Ghose, N., N. Chatterjee, and Fareeduddin (2014), *A Petrographic Atlas of Ophiolite: An example*
831 *from the eastern India-Asia collision zone*, Springer.
832 Guenthner, W. R., P. W. Reiners, R. A. Ketcham, L. Nasdala, and G. Giester (2013), Helium diffusion in
833 natural zircon: Radiation damage, anisotropy, and the interpretation of zircon (U-Th)/He
834 thermochronology, *American Journal of Science*, *313*, 145-198.
835 Guo, R., X. Hu, E. Garzanti, W. Lai, B. Yan, and C. Mark (2020), How faithfully do the geochronological
836 and geochemical signatures of detrital zircon, titanite, rutile and monazite record magmatic and
837 metamorphic events? A case study from the Himalaya and Tibet., *Earth Science Reviews*, *201*,
838 103082.
839 Hall, R. (2012), Late Jurassic-Cenozoic reconstructions of the Indonesian region and the Indian
840 Ocean, *Tectonophysics*, *570*, 1-41.
841 Handique, G. K., A. K. Sethi, and S. C. Sarma (1989), Review of Tertiary Stratigraphy of parts of Upper
842 Assam Valley., *Geol Surv India Spec Publ.*, *23*, 23-36.
843 Horstwood, M. S. A., et al. (2016), Community-Derived Standards for LA-ICP-MS U-(Th-)Pb
844 Geochronology - Uncertainty Propagation, Age Interpretation and Data Reporting, *Geostandards and*
845 *Geoanalytical Research*, *40*(3), 311-332.
846 Htut, T. (2017), Myanmar Petroleum Systems, including the offshore area, in *Myanmar: Geology,*
847 *Resources and Tectonics*, edited by A. J. Barber, K. Zaw and M. J. Crow, pp. 219-260, Geological
848 Society of London Memors.
849 Ingersoll, R. V., T. F. Bullard, R. L. Ford, J. P. Grimm, J. D. Pickle, and S. W. Sares (1984), The effect of
850 grain-size on detrital modes: A test of the Gazzi-Dickinson point-counting method., *Journal of*
851 *Sedimentary Petrology*, *54*, 103-116.
852 Lamont, T. N., M. P. Searle, B. R. Hacker, K. Htun, K. M. Htun, C. K. Morley, D. J. Waters, and R. W.
853 White (2021), Late Eocene-Oligocene granulite facies garnet-sillimanite migmatites from the Mogok
854 Metamorphic belt, Myanmar, and implications for timing of slip along the Sagaing Fault, *Lithos*, *386*.
855 Li, J.-X., W.-M. Fan, L.-Y. Zhang, T.-P. Peng, Y.-L. Sun, L. Ding, F.-L. Cai, and K. Sein (2020), Prolonged
856 Neo-Tethyan magmatic arc in Myanmar: evidence from geochemistry and Sr-Nd-Hf isotopes of
857 Cretaceous mafic-felsic intrusions in the Banmauk-Kawlin area, *international Journal of Earth*
858 *Sciences*, *109*, 649-668.
859 Li, J.-X., W.-M. Fan, L.-Y. Zhang, N. J. Evans, Y.-L. Sun, Q.-Y. Guan, T.-P. Peng, F.-L. Cai, and K. Seinf
860 (2019), Geochronology, geochemistry and Sr-Nd-Hf isotopic compositions of Late Cretaceous-Eocene
861 granites in southern Myanmar: Petrogenetic, tectonic and metallogenic implications, *Ore Geology*
862 *Reviews*, *112*(

863), 103031.
864 Li, S. H., D. J. J. van Hinsbergen, C. L. Deng, E. L. Advokaat, and R. X. Zhu (2018), Paleomagnetic
865 Constraints From the Baoshan Area on the Deformation of the Qiangtang-Sibumasu Terrane Around
866 the Eastern Himalayan Syntaxis, *Journal of Geophysical Research-Solid Earth*, *123*(2), 977-997.
867 Liang, Y.-H., S. L. Chung, D. Liu, Y. Xu, F. Y. Wu, J. H. Yang, Y. Wang, and C. H. Lo (2008), Detrital zircon
868 evidence from Burma for reorganisation of the eastern Himalayan drainage system., *American*
869 *Journal of Science*, *308*, 618-638.
870 Licht, A., L. Reisberg, C. France-Lanord, A. Naing Soe, and J. J. Jaeger (2014), Cenozoic evolution of
871 the central Myanmar drainage system: insights from sediment provenance in the Minbu sub-basin,
872 *Basin Research*, *28*, 237-251.
873 Licht, A., C. France-Lanord, L. Reisberg, C. Fontaine, A. N. Soe, and J. J. Jaeger (2013), A palaeo Tibet-
874 Myanmar connection? Reconstructing the Late Eocene drainage system of central Myanmar using a
875 multi-proxy approach, *Journal of the Geological Society*, *170*(6), 929-939.
876 Licht, A., et al. (2020), Magmatic history of central Myanmar and implications for the evolution of
877 the Burma Terrane, *Gondwana Research*, *87*, 303-319.

878 Licht, A., et al. (2018), Paleogene evolution of the Burmese forearc basin and implications for the
879 history of India-Asia convergence, *Geological Society of America Bulletin*, *doi.org/10.1130/B35002.1*.
880 Lin, T.-H., A. H. G. Mitchell, S.-L. Chung, X.-B. Tan, J.-T. Tang, T. Oo, and F.-Y. Wu (2019), Two parallel
881 magmatic belts with contrasting isotopic characteristics from southern Tibet to Myanmar: zircon U–
882 Pb and Hf isotopic constraints, *Journal of the Geological Society, London.* , *176*, 574–587.
883 Luvizotto, G., T. Zack, H. Meyer, T. Ludwig, S. Triebold, A. Kronz, C. Münker, D. Stockli, S. Prowatke,
884 and S. Klemme (2009), Rutile crystals as potential trace element and isotope mineral standards for
885 microanalysis, *Chemical Geology*, *261*(3), 346-369.
886 Maurin, T., and C. Rangin (2009), Impact of the 90 degrees E ridge at the Indo-Burmese subduction
887 zone imaged from deep seismic reflection data, *Marine Geology*, *266*(1-4), 143-155.
888 Mitchell, A. (2018), *Geological Belts, Plate Boundaries, and Mineral Deposits in Myanmar*, Elsevier,
889 ISBN: 978-0-12-803382-1.
890 Mitchell, A. H. G., T. Hlaing, and N. Htay (2010), The Chin Hills Segment of the Indo-Burman Ranges:
891 Not a simple Accretionary Wedge, *Memoir Geological Society of India*, *75*, 3-24.
892 Mitchell, A. H. G., S.-L. Chung, O. Thura, T.-S. Lin, and C.-H. Hung (2012), Zircon U-Pb ages in
893 Myanmar:magmatic-metamorphic events and the closure of a Neotethys ocean?, *Journal of Asian*
894 *Earth Sciences*, *56*, 1-23.
895 Morley, C. K. (2009), Evolution from an oblique subduction back-arc mobile belt to a highly oblique
896 collisional margin: The Cenozoic tectonic development of Thailand and eastern Myanmar.,
897 *Geological Society London Special Publication*, *318*, 373-403.
898 Morley, C. K., and F. Arboit (2019), Dating the onset of motion on the Sagaing fault: Evidence from
899 detrital zircon and titanite U-Pb geochronology from the North Minwun Basin, Myanmar, *Geology*,
900 *47*(6), 581-585.
901 Morley, C. K., T. T. Naing, M. Searle, and S. A. Robinson (2020), Structural and tectonic development
902 of the Indo-Burma ranges, *Earth-Science Reviews*, *200*.
903 Morley, C. K., S. Chantraprasert, J. Kongchum, and K. Chenoll (2021), The West Burma Terrane, a
904 review of recent paleo-latitude data, its geological implications and constraints, *Earth Science*
905 *Reviews*, *220*, 103722.
906 Naing, T. T., D. A. Bussien, W. H. Winkler, M. Nold, and A. Von Quadt (2014), Provenance study on
907 Eocene-Miocene sandstones of the Rakhine Coastal Belt, Indo-Burman Ranges of Myanmar:
908 geodynamic implications, in *Sediment Provenance Studies in Hydrocarbon Exploration and*
909 *Production*, edited by R. A. Scott, H. R. Smyth, A. C. Morton and N. Richardson, pp. 195-216.
910 Najman, Y., et al. (2020), The exhumation of the Indo-Burman Ranges, Myanmar, *Earth and*
911 *Planetary Science Letters*, *530*.
912 Najman, Y., et al. (2008), The Paleogene record of Himalayan erosion: Bengal Basin, Bangladesh,
913 *Earth and Planetary Science Letters*, *273*(1-2), 1-14.
914 Parra, M., A. Mora, E. R. Sobel, M. R. Strecker, and R. González (2009), Episodic orogenic front
915 migration in the northern Andes: Constraints from low-temperature thermochronology in the
916 Eastern Cordillera, Colombia, *Tectonics*, *28*, TC4004, doi:4010.1029/2008TC002423.
917 Paton, C., J. Hellstrom, B. Paul, J. Woodhead, and J. Hergt (2011), Iolite: Freeware for the
918 visualisation and processing of mass spectrometric data, *Journal of Analytical Atomic Spectrometry*,
919 *26*(12), 2508-2518.
920 Rangin, C., T. Maurin, and F. Masson (2013), Combined effects of Eurasia/Sunda oblique
921 convergence and East-Tibetan crustal flow on the active tectonics of Burma., *Journal of Asian Earth*
922 *Sciences*, *76*, 185-194.
923 Reiners, P. W., and M. T. Brandon (2006), Using thermochronology to understand orogenic erosion,
924 *Annual Review of Earth and Planetary Sciences*, *34*, 419-466.
925 Robinson, R. A. J., C. A. Brezina, R. R. Parrish, M. S. A. Horstwood, N. W. Oo, M. I. Bird, M. Thein, A. S.
926 Walters, G. J. H. Oliver, and K. Zaw (2014), Large rivers and orogens: The evolution of the Yarlung
927 Tsangpo-Irrawaddy system and the eastern Himalayan syntaxis, *Gondwana Research*, *26*(1), 112-
928 121.

Searle, M. P., J. M. Garber, B. R. Hacker, K. Htun, N. J. Gardiner, D. J. Waters, and L. J. Robb (2020), Timing of Syenite-Charnockite Magmatism and Ruby and Sapphire Metamorphism in the Mogok Valley Region, Myanmar, *Tectonics*, *39*(3).
Sevastjanova, I., R. Hall, M. Rittner, S. Paw, T. T. Naing, D. H. Alderton, and G. Comfrt (2015), Myanmar and Asia United, Australia left behind long ago., *Gondwana Research*, *in press*.
Sláma, J., J. Košler, D. J. Condon, J. L. Crowley, A. Gerdes, J. M. Hanchar, M. S. Horstwood, G. A. Morris, L. Nasdala, and N. Norberg (2008), Plešovice zircon—a new natural reference material for U–Pb and Hf isotopic microanalysis, *Chemical Geology*, *249*(1), 1-35.
Sobel, E. R., and M. R. Strecker (2003), Uplift, exhumation and precipitation: tectonic and climatic control of Late Cenozoic landscape evolution in the northern Sierras Pampeanas, Argentina, *Basin Research*, *15*(4), 431-451.
Socquet, A., B. Goffe, M. Pubellier, and C. Ragin (2002), Le metamorphism Tardi-Cretace a Eocene des zones internes de la chaine Indo-Birmane (Myanmar occidental):implications geodynamiques, *C.R. Geoscience*, *334*, 573-580.
Verard, C., G. Stampfli, G. Borel, and C. Hochard (2017), The Indian promontory: A bridge between plate tectonics and life evolution models., *Universal Journal of Geoscience*, *5*, 25-32.
Vermeesch, P. (2018), IsoplotR: a free and open toolbox for geochronology., *Geoscience Frontiers*, *9*, 1479-1493.
Wang, J. G., F. Y. Wu, X. C. Tan, and C. Z. Liu (2014), Magmatic evolution of the Western Myanmar Arc documented by U-Pb and Hf isotopes in detrital zircon, *Tectonophysics*, *612*, 97-105.
Westerweel, J. (2020), The India-Asia Collision from the Perspective of Myanmar: Insights from Paleomagnetism and Paleogeographic Reconstructions, 287 pp, University of Rennes.
Westerweel, J., P. Roperch, A. Licht, G. Dupont-Nivet, Z. Win, F. Poblete, G. Ruffet, H. H. Swe, M. K. Thi, and D. W. Aung (2019), Burma Terrane part of the Trans-Tethyan arc during collision with India according to palaeomagnetic data, *Nature Geoscience*, *12*(10), 863-+.
Westerweel, J., A. Licht, N. Cogne, P. Roperch, G. Dupont-Nivet, M. K. Thi, H. H. Swe, H. S. Huang, Z. Win, and D. W. Aung (2020), Burma Terrane Collision and Northward Indentation in the Eastern Himalayas Recorded in the Eocene-Miocene Chindwin Basin (Myanmar), *Tectonics*, *39*(10).
Wiedenbeck, M., P. Alle, F. Corfu, W. Griffin, M. Meier, F. Oberli, A. v. Quadt, J. Roddick, and W. Spiegel (1995), Three natural zircon standards for U-Th-Pb, Lu-Hf, trace element and REE analyses, *Geostandards newsletter*, *19*(1), 1-23.
Yao, W., L. Ding, F. Cai, H. Wang, Q. Xu, and T. Zaw (2017), Origin and tectonic evolution of upper Triassic Turbidites in the Indo-Burman ranges, West Myanmar, *Tectonophysics*, *721*, 90-105.
Zack, T., D. F. Stockli, G. L. Luvizotto, M. G. Barth, E. Belousova, M. R. Wolfe, and R. W. Hinton (2011), In situ U-Pb rutile dating by LA-ICP-MS: 208Pb correction and prospects for geological applications. , *Contributions to Mineralogy and Petrology*, *162*, 515– 530.
Zhang, J., W. Xiao, B. F. Windley, F. Cai, K. Sein, and S. Naing (2017), Early Cretaceous wedge extrusion in the Indo-Burma Range accretionary complex: implications for the Mesozoic subduction of Neothethys in SE Asia, *International Journal of Earth Sciences*, *106*, 1391-1408.
Zhang, P., L. F. Mei, X. L. Hu, R. Y. Li, L. L. Wu, Z. C. Zhou, and H. N. Qiu (2017), Structures, uplift, and magmatism of the Western Myanmar Arc: Constraints to mid-Cretaceous-Paleogene tectonic evolution of the western Myanmar continental margin, *Gondwana Research*, *52*, 18-+.
Zhang, P., L. F. Mei, S. Y. Jiang, S. H. Xu, R. A. Donelick, R. Y. Li, and H. Zhang (2021), Erosion and sedimentation in SE Tibet and Myanmar during the evolution of the Burmese continental margin from the Late Cretaceous to Early Neogene, *Gondwana Research*, *95*, 149-175.
Zhang, P., et al. (2019), Palaeodrainage evolution of the large rivers of East Asia and Himalayan-Tibet tectonics., *Earth Science Reviews*, *In press*.
Zhao, S.-W., S.-C. Lai, J.-F. Qin, R.-Z. Zhu, and J.-B. Wang (2017), Geochemical and geochronological characteristics of Late Cretaceous to Early Paleocene granitoids in the Tengchong Block, Southwestern China: Implications for crustal anatexis and thickness variations along the eastern Neo-Tethys subduction zone, *Tectonophysics*, *694*, 87-100.

980 Zhou, R., L. M. Schoenbohm, E. Sobel, D. W. Davis, and J. Glodny (2017), New constraints on
981 orogenic models of the southern Central Andean Plateau: Cenozoic basin evolution and bedrock
982 exhumation, *Geological Society of America Bulletin*, *129*, 152-170.

983

Figure 1.

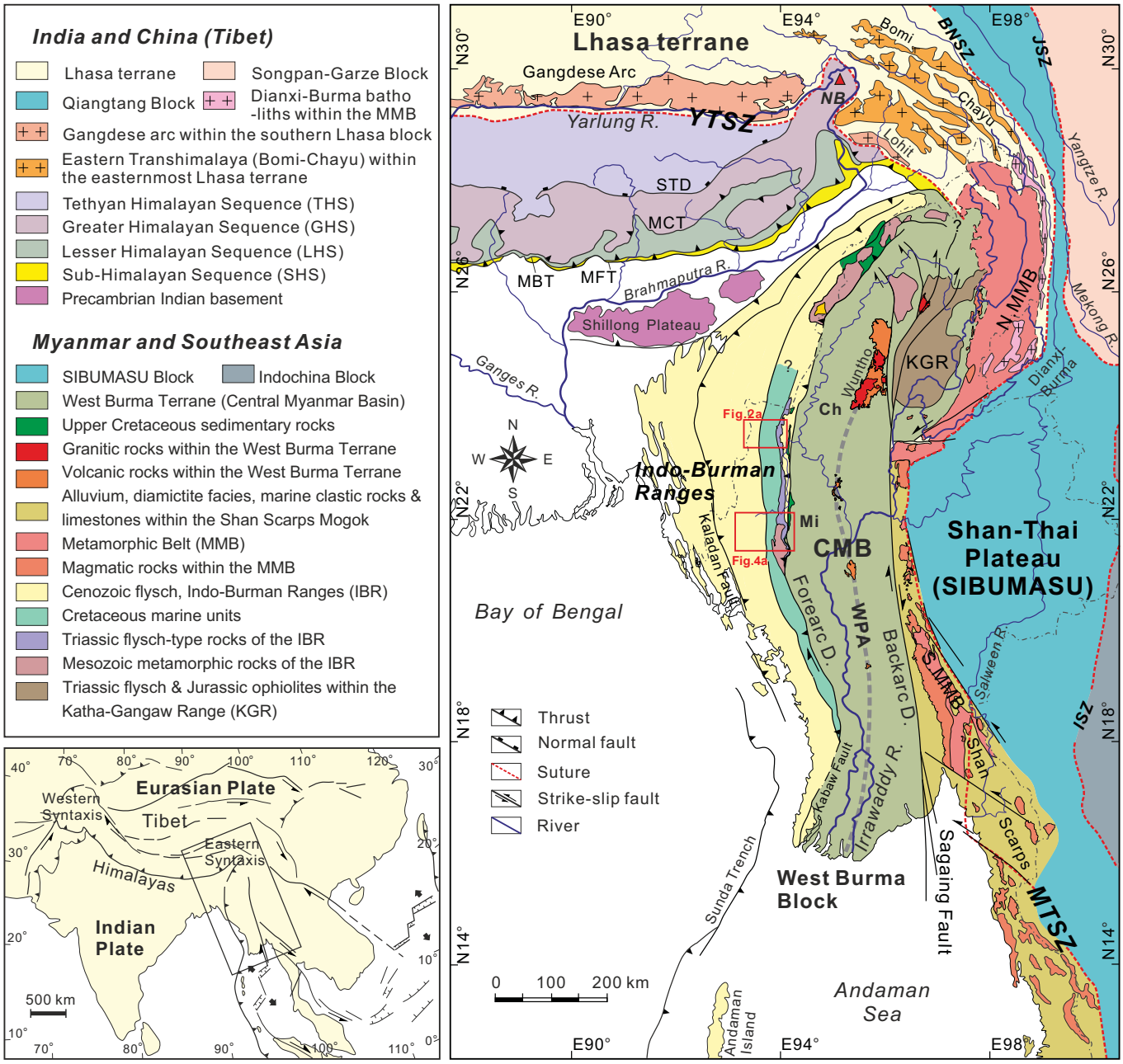
India and China (Tibet)
Lhasa terrane
Songpan-Garze Block
Qiangtang Block
Dianxi-Burma batho -liths within the MMB
Gangdese arc within the southern Lhasa block
Eastern Transhimalaya (Bomi-Chayu) within the easternmost Lhasa terrane
Tethyan Himalayan Sequence (THS)
Greater Himalayan Sequence (GHS)
Lesser Himalayan Sequence (LHS)
Sub-Himalayan Sequence (SHS)
Precambrian Indian basement
Myanmar and Southeast Asia
SIBUMASU Block
Indochina Block
West Burma Terrane (Central Myanmar Basin)
Upper Cretaceous sedimentary rocks
Granitic rocks within the West Burma Terrane
Volcanic rocks within the West Burma Terrane
Alluvium, diamictite facies, marine clastic rocks & limestones within the Shan Scarps Mogok
Metamorphic Belt (MMB)
Magmatic rocks within the MMB
Cenozoic flysch, Indo-Burman Ranges (IBR)
Cretaceous marine units
Triassic flysch-type rocks of the IBR
Mesozoic metamorphic rocks of the IBR
Triassic flysch & Jurassic ophiolites within the Katha-Gangaw Range (KGR)
Eurasian Plate
Tibet
Western Syntaxis
Eastern Syntaxis
Himalayas
Indian Plate
500 km
Lhasa terrane
Gangdese Arc
Yarlung R.
YTSZ
NB
Bomi
Chayu
Lohit
BNSZ
JSZ
Yangtze R.
STD
MCT
MBT
MFT
Brahmaputra R.
Shillong Plateau
Ganges R.
Mekong R.
N.MMB
KGR
Wuntho
Ch
Dianxi-Burma
Fig.2a
Indo-Burman Ranges
Mi
CMB
Fig.4a
Kaladan Fault
Bay of Bengal
Forearc D.
WPA
Backarc D.
Irrawaddy R.
Kabaw Fault
Sunda Trench
West Burma Block
Sagaing Fault
S.MMB
Salween R.
Shan Scarps
MTSZ
ZSZ
Shan-Thai Plateau (SIBUMASU)
Andaman Sea
Andaman Island
Thrust
Normal fault
Suture
Strike-slip fault
River
0 100 200 km
N
W
E
S
E90°
E94°
E98°
N30°
N26°
N22°
N18°
N14°

Figure 2.

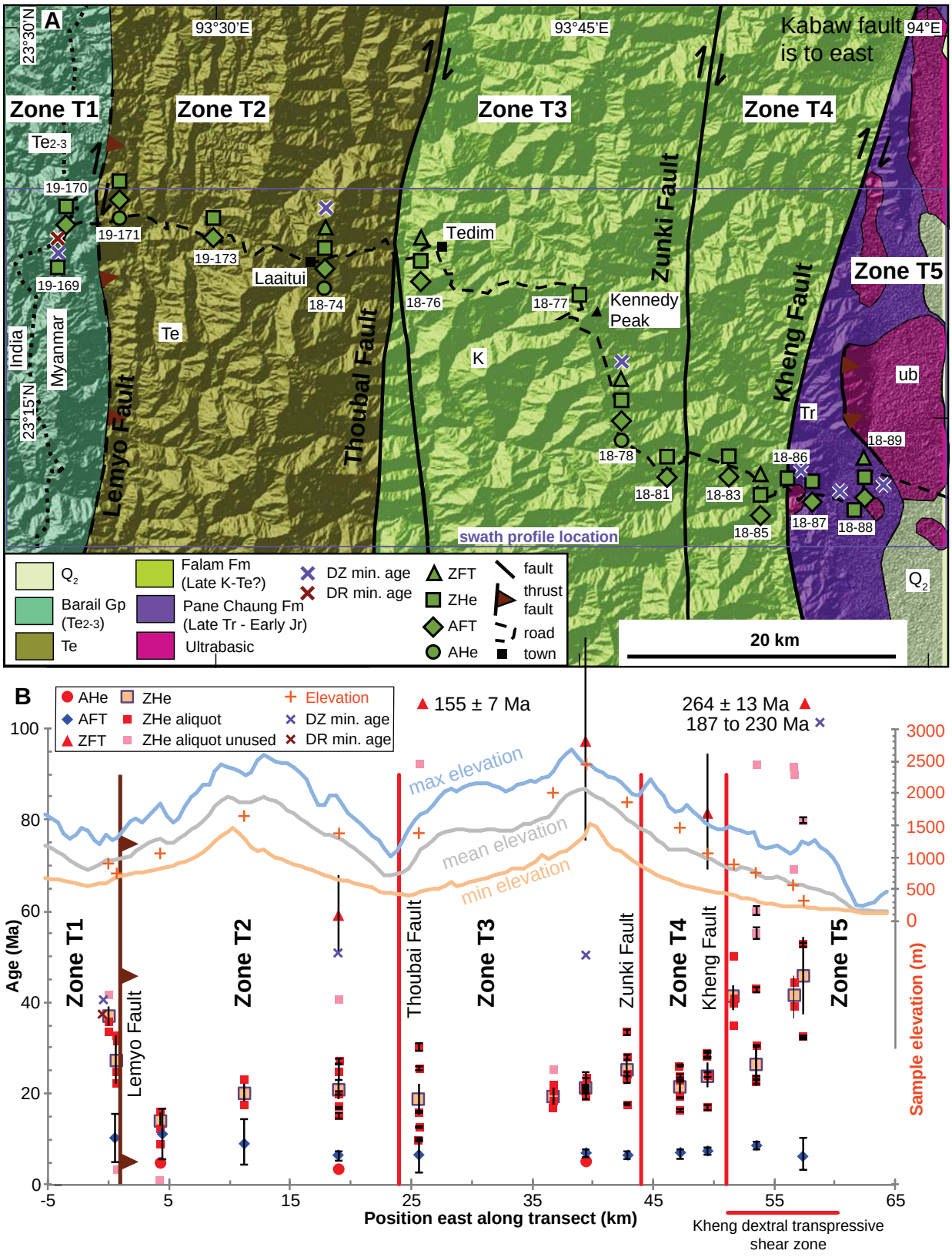
A
23°30'N
93°30'E
93°45'E
94°E
Kabaw fault is to east
Zone T1
Zone T2
Zone T3
Zone T4
Zone T5
Te2-3
19-170
19-171
19-173
19-169
Laaitui
18-74
Tedim
18-76
18-77
Kennedy Peak
Zunki Fault
Kheng Fault
Lemyo Fault
Thoubal Fault
India
Myanmar
23°15'N
Te
K
ub
Tr
18-78
18-81
18-83
18-85
18-86
18-87
18-88
18-89
swath profile location
Q2
Barail Gp (Te2-3)
Te
Falam Fm (Late K-Te?)
Pane Chaung Fm (Late Tr - Early Jr)
Ultrabasic
DZ min. age
DR min. age
ZFT
ZHe
AFT
AHe
fault
thrust fault
road
town
20 km
B
AHe
ZHe
Elevation
AFT
ZHe aliquot
DZ min. age
ZFT
ZHe aliquot unused
DR min. age
155 ± 7 Ma
264 ± 13 Ma
187 to 230 Ma
max elevation
mean elevation
min elevation
Age (Ma)
Sample elevation (m)
Zone T1
Zone T2
Zone T3
Zone T4
Zone T5
Lemyo Fault
Thoubai Fault
Zunki Fault
Kheng Fault
Position east along transect (km)
Kheng dextral transpressive shear zone

Figure 3.

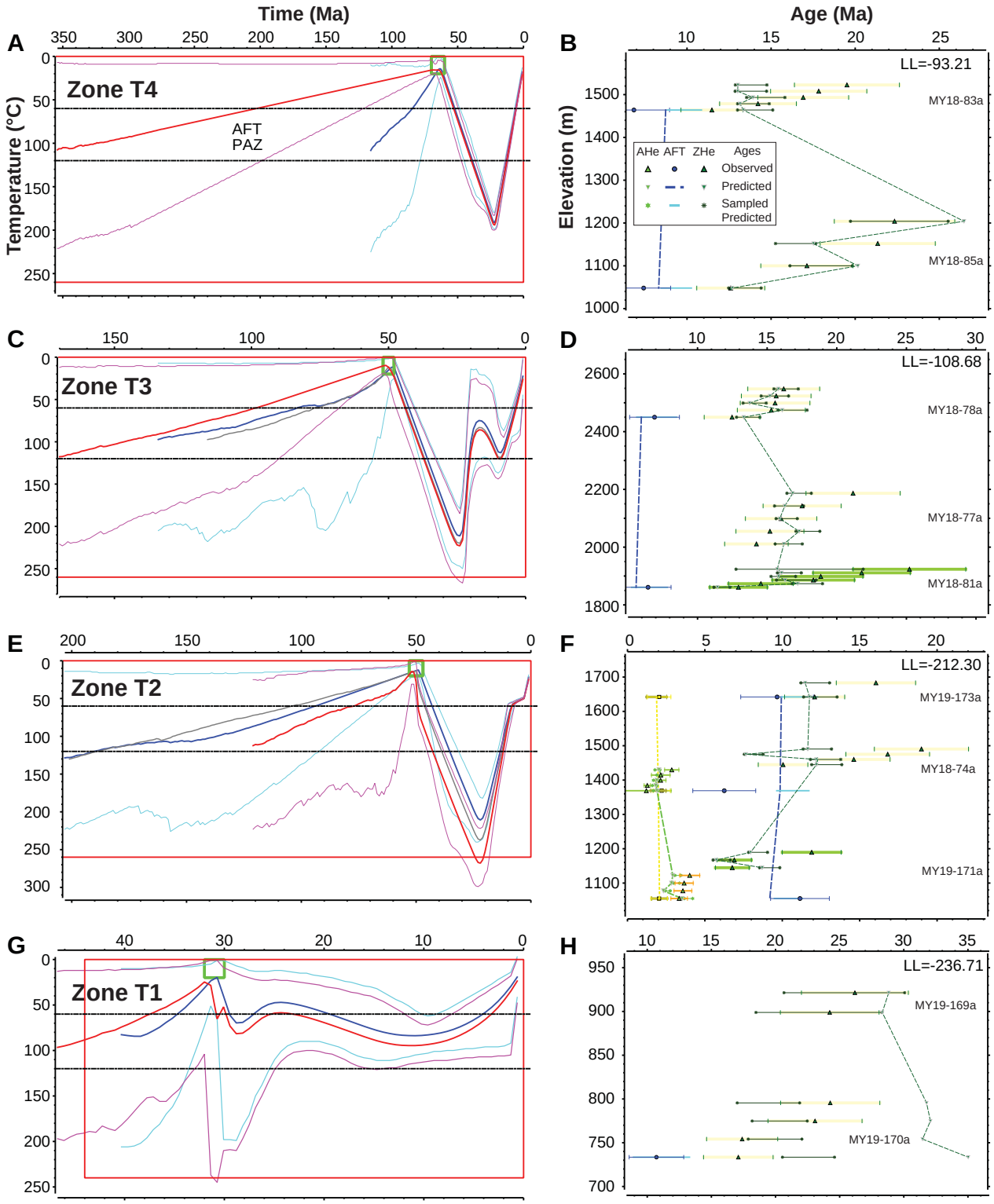
A
Time (Ma)
Temperature (°C)
Zone T4
AFT
PAZ
B
Age (Ma)
Elevation (m)
LL=-93.21
MY18-83a
MY18-85a
AHe AFT ZHe Ages
Observed
Predicted
Sampled
Predicted
C
Zone T3
D
LL=-108.68
MY18-78a
MY18-77a
MY18-81a
E
Zone T2
F
LL=-212.30
MY19-173a
MY18-74a
MY19-171a
G
Zone T1
H
LL=-236.71
MY19-169a
MY19-170a

Figure 4.

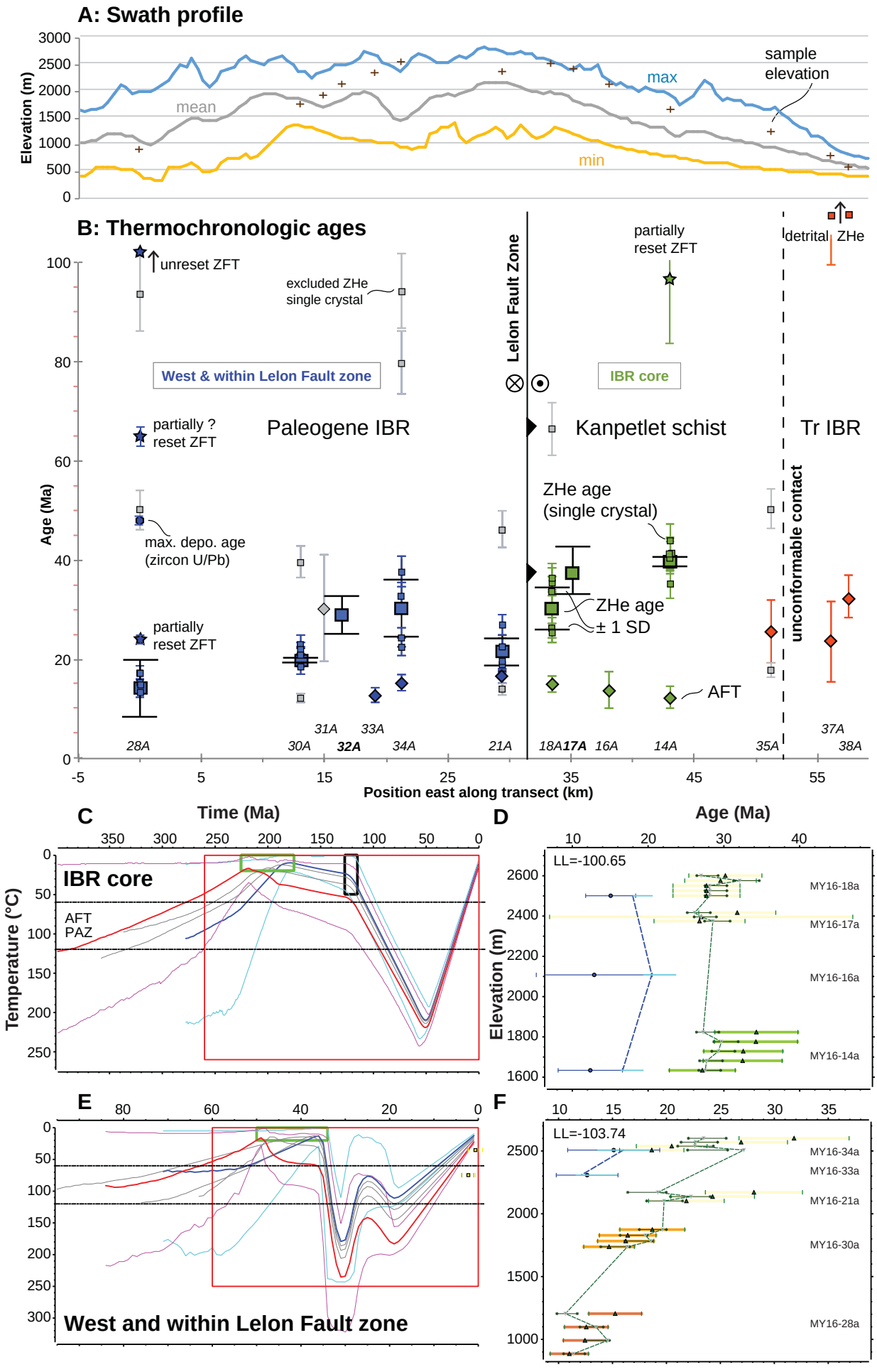
A: Swath profile
Elevation (m)
3000
2500
2000
1500
1000
500
0
max
mean
min
sample elevation
B: Thermochronologic ages
Age (Ma)
100
80
60
40
20
0
unreset ZFT
excluded ZHe single crystal
West & within Lelon Fault zone
partially ? reset ZFT
Paleogene IBR
max. depo. age (zircon U/Pb)
partially reset ZFT
Lelon Fault Zone
partially reset ZFT
IBR core
Kanpetlet schist
Tr IBR
detrital ZHe
ZHe age (single crystal)
ZHe age ± 1 SD
AFT
unconformable contact
28A
30A
31A
32A
33A
34A
21A
18A
17A
16A
14A
35A
37A
38A
-5
5
15
25
35
45
55
Position east along transect (km)
C
Time (Ma)
350
300
250
200
150
100
50
0
IBR core
AFT
PAZ
Temperature (°C)
0
50
100
150
200
250
D
Age (Ma)
10
20
30
40
LL=-100.65
Elevation (m)
2600
2400
2200
2000
1800
1600
MY16-18a
MY16-17a
MY16-16a
MY16-14a
E
80
60
40
20
0
0
50
100
150
200
250
300
West and within Lelon Fault zone
F
10
15
20
25
30
35
LL=-103.74
2500
2000
1500
1000
MY16-34a
MY16-33a
MY16-21a
MY16-30a
MY16-28a

Figure 5.

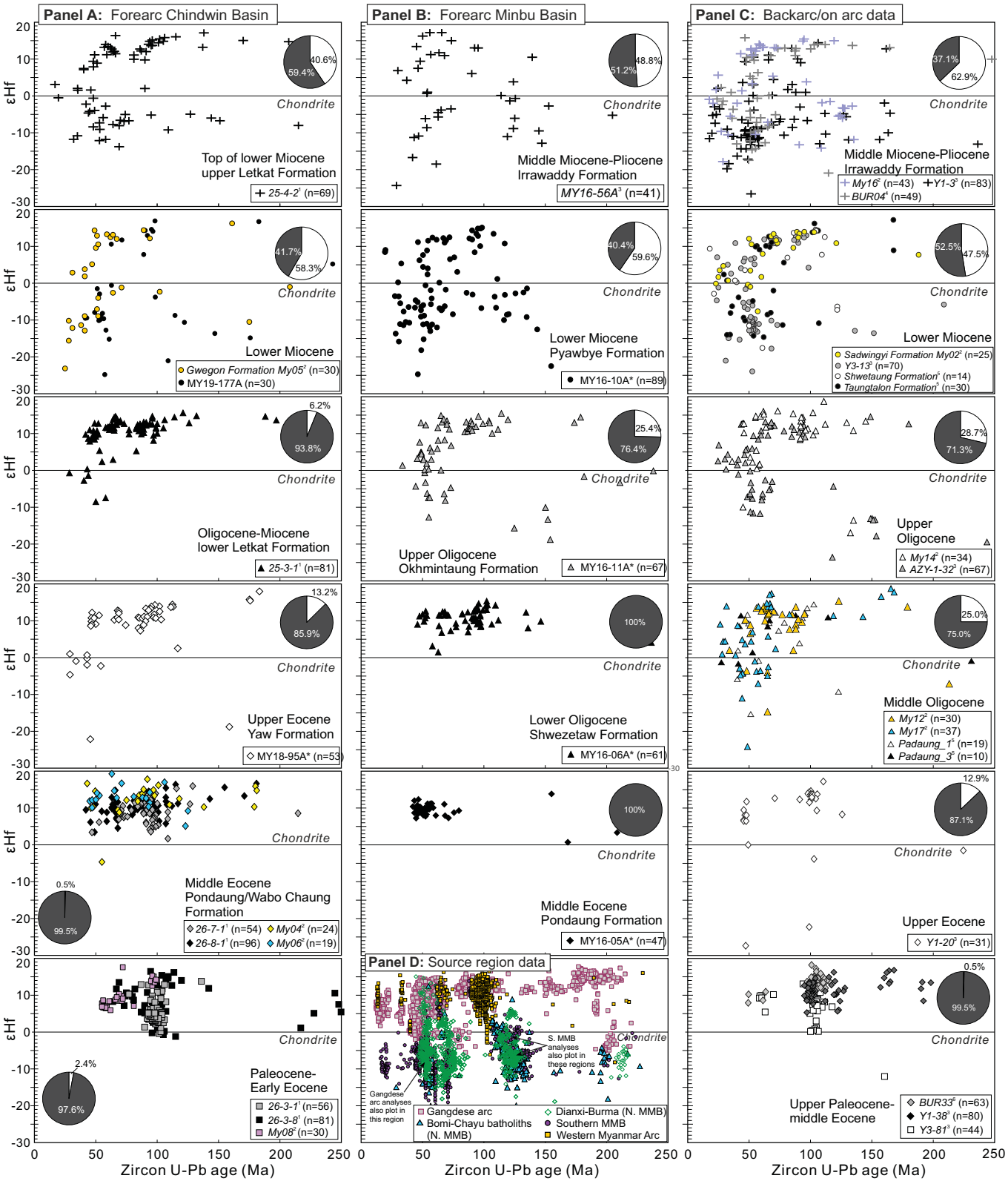
Panel A: Forearc Chindwin Basin
Panel B: Forearc Minbu Basin
Panel C: Backarc/on arc data
Panel D: Source region data
εHf
Chondrite
Top of lower Miocene upper Letkat Formation
25-4-2 (n=69)
40.6%
59.4%
Middle Miocene-Pliocene Irrawaddy Formation
MY16-56A (n=41)
48.8%
51.2%
Middle Miocene-Pliocene Irrawaddy Formation
My16 (n=43)
Y1-3 (n=83)
BUR04 (n=49)
37.1%
62.9%
Lower Miocene
Gwegon Formation My05 (n=30)
MY19-177A (n=30)
41.7%
58.3%
Lower Miocene Pyawbye Formation
MY16-10A* (n=89)
40.4%
59.6%
Lower Miocene
Sadwingyi Formation My02 (n=25)
Y3-13 (n=70)
Shwetaung Formation (n=14)
Taungtalon Formation (n=30)
52.5%
47.5%
Oligocene-Miocene lower Letkat Formation
25-3-1 (n=81)
6.2%
93.8%
Upper Oligocene Okhmintaung Formation
MY16-11A* (n=67)
25.4%
76.4%
Upper Oligocene
My14 (n=34)
AZY-1-32 (n=67)
28.7%
71.3%
Upper Eocene Yaw Formation
MY18-95A* (n=53)
13.2%
85.9%
Lower Oligocene Shwezetaw Formation
MY16-06A* (n=61)
100%
Middle Oligocene
My12 (n=30)
My17 (n=37)
Padaung_1 (n=19)
Padaung_3 (n=10)
25.0%
75.0%
Middle Eocene Pondaung/Wabo Chaung Formation
26-7-1 (n=54)
My04 (n=24)
26-8-1 (n=96)
My06 (n=19)
0.5%
99.5%
Middle Eocene Pondaung Formation
MY16-05A* (n=47)
100%
Upper Eocene
Y1-20 (n=31)
12.9%
87.1%
Paleocene-Early Eocene
26-3-1 (n=56)
26-3-8 (n=81)
My08 (n=30)
2.4%
97.6%
Gangdese arc analyses also plot in this region
S. MMB analyses also plot in these regions
Gangdese arc
Bomi-Chayu batholiths (N. MMB)
Dianxi-Burma (N. MMB)
Southern MMB
Western Myanmar Arc
Upper Paleocene-middle Eocene
BUR33 (n=63)
Y1-38 (n=80)
Y3-81 (n=44)
0.5%
99.5%
Zircon U-Pb age (Ma)

Figure 6.

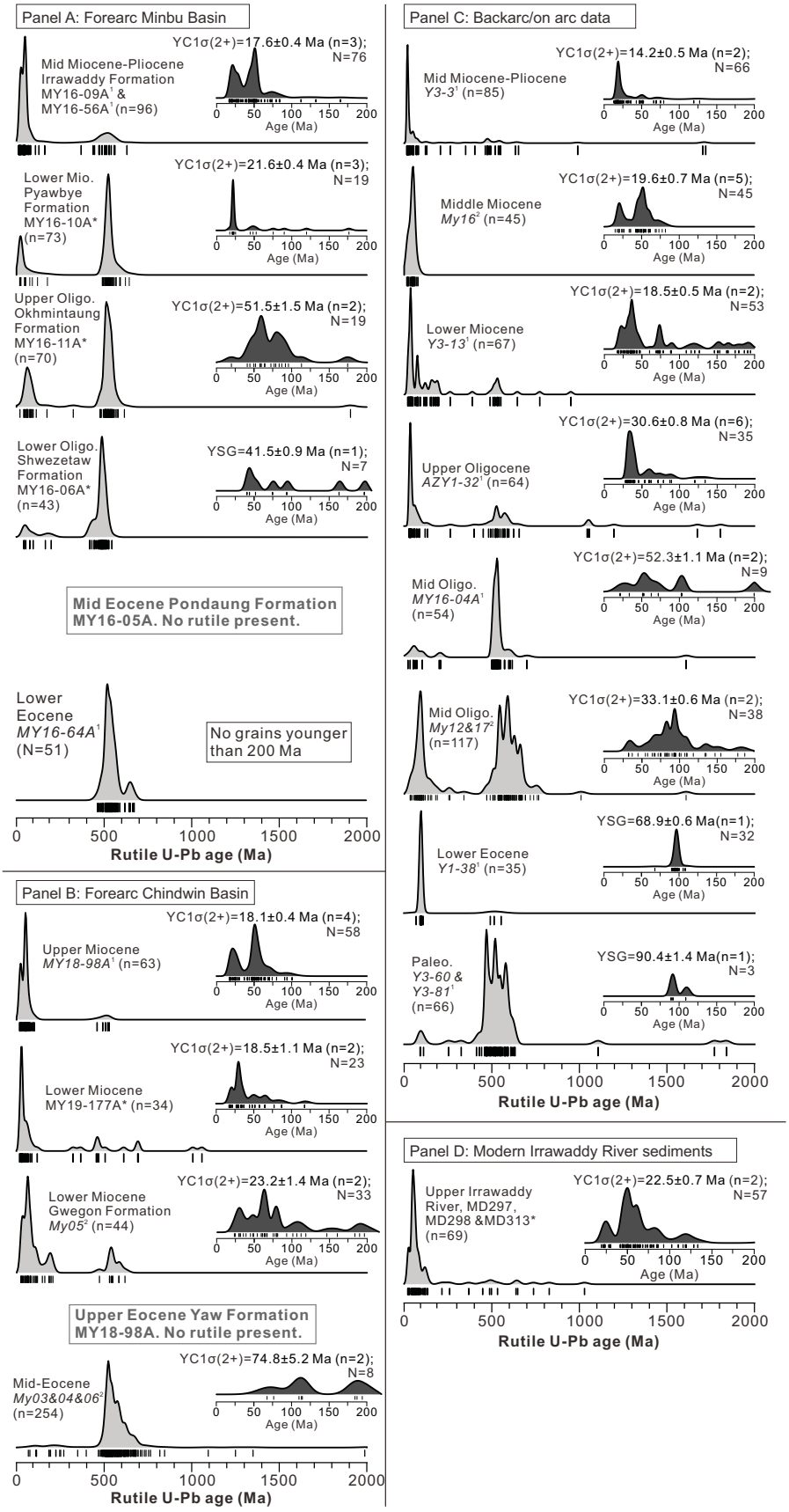
Panel A: Forearc Minbu Basin
YC1σ(2+)=17.6±0.4 Ma (n=3); N=76
Mid Miocene-Pliocene Irrawaddy Formation MY16-09A[1] & MY16-56A[1] (n=96)
YC1σ(2+)=21.6±0.4 Ma (n=3); N=19
Lower Mio. Pyawbye Formation MY16-10A* (n=73)
YC1σ(2+)=51.5±1.5 Ma (n=2); N=19
Upper Oligo. Okhmintaung Formation MY16-11A* (n=70)
YSG=41.5±0.9 Ma (n=1); N=7
Lower Oligo. Shwezetaw Formation MY16-06A* (n=43)
Mid Eocene Pondaung Formation MY16-05A. No rutile present.
Lower Eocene MY16-64A[1] (N=51)
No grains younger than 200 Ma
Rutile U-Pb age (Ma)
Panel B: Forearc Chindwin Basin
YC1σ(2+)=18.1±0.4 Ma (n=4); N=58
Upper Miocene MY18-98A[1] (n=63)
YC1σ(2+)=18.5±1.1 Ma (n=2); N=23
Lower Miocene MY19-177A* (n=34)
YC1σ(2+)=23.2±1.4 Ma (n=2); N=33
Lower Miocene Gwegon Formation My05[2] (n=44)
Upper Eocene Yaw Formation MY18-98A. No rutile present.
YC1σ(2+)=74.8±5.2 Ma (n=2); N=8
Mid-Eocene My03&04&06[2] (n=254)
Rutile U-Pb age (Ma)
Panel C: Backarc/on arc data
YC1σ(2+)=14.2±0.5 Ma (n=2); N=66
Mid Miocene-Pliocene Y3-3[1] (n=85)
YC1σ(2+)=19.6±0.7 Ma (n=5); N=45
Middle Miocene My16[2] (n=45)
YC1σ(2+)=18.5±0.5 Ma (n=2); N=53
Lower Miocene Y3-13[1] (n=67)
YC1σ(2+)=30.6±0.8 Ma (n=6); N=35
Upper Oligocene AZY1-32[1] (n=64)
YC1σ(2+)=52.3±1.1 Ma (n=2); N=9
Mid Oligo. MY16-04A[1] (n=54)
YC1σ(2+)=33.1±0.6 Ma (n=2); N=38
Mid Oligo. My12&17[2] (n=117)
YSG=68.9±0.6 Ma(n=1); N=32
Lower Eocene Y1-38[1] (n=35)
YSG=90.4±1.4 Ma(n=1); N=3
Paleo. Y3-60 & Y3-81[1] (n=66)
Rutile U-Pb age (Ma)
Panel D: Modern Irrawaddy River sediments
YC1σ(2+)=22.5±0.7 Ma (n=2); N=57
Upper Irrawaddy River, MD297, MD298 &MD313* (n=69)
Rutile U-Pb age (Ma)
Age (Ma)

Fig 6